Hindawi
Geofluids
Volume 2018, Article ID 1789278, 20 pages
https://doi.org/10.1155/2018/1789278

Research Article

Dynamic Behavior of CO_2 in a Wellbore and Storage Formation: Wellbore-Coupled and Salt-Precipitation Processes during Geologic CO_2 Sequestration

Jize Piao,[1] **Weon Shik Han**,[1] **Sungwook Choung**,[2] **and Kue-Young Kim**[3]

[1]*Department of Earth System Sciences, Yonsei University, Seoul, Republic of Korea*
[2]*Division of Earth and Environmental Sciences, Korea Basic Science Institute (KBSI), Cheongju, Republic of Korea*
[3]*Korea Institute of Geoscience and Mineral Resources, Daejeon, Republic of Korea*

Correspondence should be addressed to Weon Shik Han; hanw@yonsei.ac.kr

Received 29 July 2017; Revised 15 November 2017; Accepted 19 December 2017; Published 29 January 2018

Academic Editor: Stefan Finsterle

For investigating the wellbore flow process in CO_2 injection scenarios, coupled wellbore-reservoir (WR) and conventional equivalent porous media (EPM) models were compared with each other. In WR model, during the injection, conditions for the wellbore including pressure and temperature were dynamically changed from the initial pressure (7.45–8.33 MPa) and temperature (52.0–55.9°C) of the storage formation. After 3.35 days, the wellbore flow reached the steady state with adiabatic condition; temperature linearly increased from the well-head (35°C) to the well-bottom (52°C). In contrast, the EPM model neglecting the wellbore process revealed that CO_2 temperature was consistently 35°C at the screen interval. Differences in temperature from WR and EPM models resulted in density contrast of CO_2 that entered the storage formation (~200 and ~600 kg/m^3, resp.). Subsequently, the WR model causing greater density difference between CO_2 and brine revealed more vertical CO_2 migration and counterflow of brine and also developed the localized salt-precipitation. Finally, a series of sensitivity analyses for the WR model was conducted to assess how the injection conditions influenced interplay between flow system and the localized salt-precipitation in the storage formation.

1. Introduction

As an approach for decreasing CO_2 emissions into the atmosphere, geologic carbon storage (GCS) is one of considerable solutions for relieving global climate change [1]. While operating GCS projects, CO_2, directly captured during industrial processes at fossil-fuel power plants, was injected through the wellbore and stored within the specific geologic formation covered by low-permeability caprock [2–4]. Until now, numerous GCS projects have been or are being conducted at various scales around the world to validate the safety of GCS technology [5]. For example, several pilot-scale projects were successfully completed CO_2 injection at a rate of 10,000 metric tons per year; these projects included Frio, Texas [6], Nagaoka, Japan [7], Ketzin, and Germany [8] as well as Regional Carbon Sequestration Partnership's (RCSP) Phase II program implemented by the US Department of Energy [9, 10]. In addition to pilot-scale projects, commercial-scale projects where CO_2 was injected at an approximate rate of 1 million metric tons per year were completed or also in operation: Sleipner project in North Sea [11], Weyburn CO_2-EOR Project in Canada [12], In Salah Project in Algeria [13], and Illinois Basin-Decatur Project which is one of the Phase III projects of US Department of Energy's RCSP [14].

During the demonstration of such pilot- or commercial-scale GCS projects, transported CO_2 from the sources (e.g., coal-based power plants) must be injected through the wellbore, which is the pathway connecting the ground surface to the targeted subsurface formation [15]. Here, the wellbore is the connected open pipe while the subsurface formation is regarded as porous media. Due to the difference in their inherent configurations, within the wellbore, the inertial force is much greater than the viscous force, implying that Reynold's number can be significantly large [16]. Solution approaches to solving CO_2 transport are also different in each other. Within the wellbore, CO_2 transport belongs to the pipe

flow, which requires a solution of the Navier-Stocks equation [17]. On the other hand, once CO_2 enters porous storage formations, CO_2 transport must be explained by Darcy's law [18]. Furthermore, CO_2 injection wells were typically drilled over 1 km while penetrating multiple geologic formations. Therefore, while CO_2 migrated through the wellbore, large variations in pressure and temperature could cause to change in CO_2 phase and its thermophysical properties [19, 20].

As described, due to complexities involved during the wellbore processes, a number of studies previously drew attention and suggested that, during the CO_2 injection activity, profiles of both pressure and temperature in the wellbore could change dynamically [21–27]. For example, Lu and Connell [21] suggested that the wellbore fluids could exhibit multiphase (supercritical, liquid, gaseous CO_2, and brine) concurrently experiencing their phase changes. Furthermore, both CO_2 and brine could experience thermal alteration caused by frictional loss, thermal conduction, convection, and Joul-Thomson heating/cooling [22, 27–29]. Due to such complex alteration processes, both bottom-hole pressure and temperature would be significantly different from ones at the well-head. Subsequently, altered pressure and temperature profiles would significantly affect thermophysical properties of CO_2 such as density, viscosity, enthalpy, internal energy, and solubility [19, 26, 30–32].

When thermophysically altered CO_2 entered the storage formation, the brine within porous media would be displaced. Subsequently, the dry-out zone would be developed in the vicinity of the injection well where residual brine evaporated to dry-CO_2 while precipitating the solid salt [33, 34]. Previously, numerous studies including both experimental [35–37] and numerical studies [34, 38–41] evaluated development of dry-out zone and associated salt-precipitation. Among them, Oh et al. [36] conducted core-flooding experiments and captured the salt-precipitation at the core-inlet by using SEM images. In addition, Kim et al. [39] and Guyant et al. [40] used numerical approach to elaborate the salt-precipitation processes according to conditions for both the injection well and storage formation. In particular, within low injection rate and high permeability of the storage formation, buoyancy effect on CO_2 became dominant, and consequently, the localized salt-precipitation was developed [41] concurrently elevating pressure around the injection well [42]. Most importantly, development of the localized salt was dependent on the degree of buoyancy force on CO_2 plume, which was governed by the injection rate and thermophysical properties of CO_2. Even though thermophysical CO_2 properties could be changed significantly after CO_2 experiencing the wellbore processes, only a few studies were considered the wellbore processes impacting on CO_2 behavior in the storage formation [22, 24, 43–45].

For example, a number of previous studies neglected the wellbore flow process or interpreted the wellbore flow by adopting Darcy's law after assigning adequate rock properties [46–48]. This approach is called equivalent porous media (EPM) model. The primary reason for such simplification arises from technical difficulties solving both the wellbore and porous media flow at the same time. Nevertheless, it is recognized that fully coupled wellbore-reservoir models, capable of accounting for nonisothermal two-phase (CO_2 and brine or water) flow, are necessary to evaluate the influence of wellbore flow on injected CO_2 within the storage formation [44, 49]. Due to this reason, the purpose of this study was to advance current understanding related to the wellbore flow process by investigating the change of both pressure and temperature profiles within the wellbore, and subsequently, CO_2 migration, and resulting accumulation of solid salt in the storage formation.

2. Method

2.1. Conceptual Model. In order to evaluate differences between equivalent porous media (EPM) and coupled wellbore-reservoir (WR) models, two base-cases which were two-dimensional radially symmetric and nonisothermal models (Case 1 and Case 2) were employed (Figures 1(a) and 1(b)). Case 1 adopted the conventional EPM approach for simulating both an injection well and a storage formation while Case 2 utilized the WR model for simulating the injection well which coupled to the storage formation. In both cases, CO_2 was injected into the storage formation which was the 40 m thick high-permeability (k) formation ($k = 3 \times 10^{-13}\,m^2$ and $\phi = 0.25$) overlaid by the 50 m thick low-k sealing caprock ($k = 1 \times 10^{-17}\,m^2$ and $\phi = 0.2$). These formations were positioned at a depth of 690 m below the ground surface, and their radial extent was 10,000 m. The storage formation was divided vertically into 10 layers (each layer with 4 m thickness) while the overlying sealing formation was divided into 5 layers having individually 10 m thickness. Then, they were horizontally discretized to 200 columns with the logarithmic increment from the injection well; the specific number and size of grid-blocks to the radial direction are shown in Figure 1.

For the initial condition, the hydrostatic pressure was assigned with the gradient of 10.58 kPa/m (top: 7.45 MPa to bottom: 8.33 MPa), and the geothermal gradient of 0.046°C/m was assigned with assuming the surface temperature of 20°C (model top: 52.0°C to bottom: 55.9°C). In addition, the dissolved NaCl mass fraction in the ambient brine was uniformly 15% with zero CO_2 saturation. For the boundary conditions, both top and bottom boundaries were assigned to be no-flow condition without assigning the conductive heat flow at the bottom boundary; temperature field in the model was dominantly governed by the geothermal gradient assigned to lateral boundaries. The conductive heat flows were neglected because buoyant CO_2 plume holding different temperature typically governed the temperature field adjacent to CO_2 plume and the injection well. Furthermore, the right-most side of the targeted formation at 10,000 m was set to be the Dirichlet boundary. By assuming the Dirichlet boundary, it was expected that the pressure pulse after reaching this boundary would be affected.

The primary difference between Case 1 and Case 2 was the condition for the left boundary assigned to the storage formation where CO_2 was injected. In Case 1 (EPM model), without the wellbore, CO_2 was injected into 10

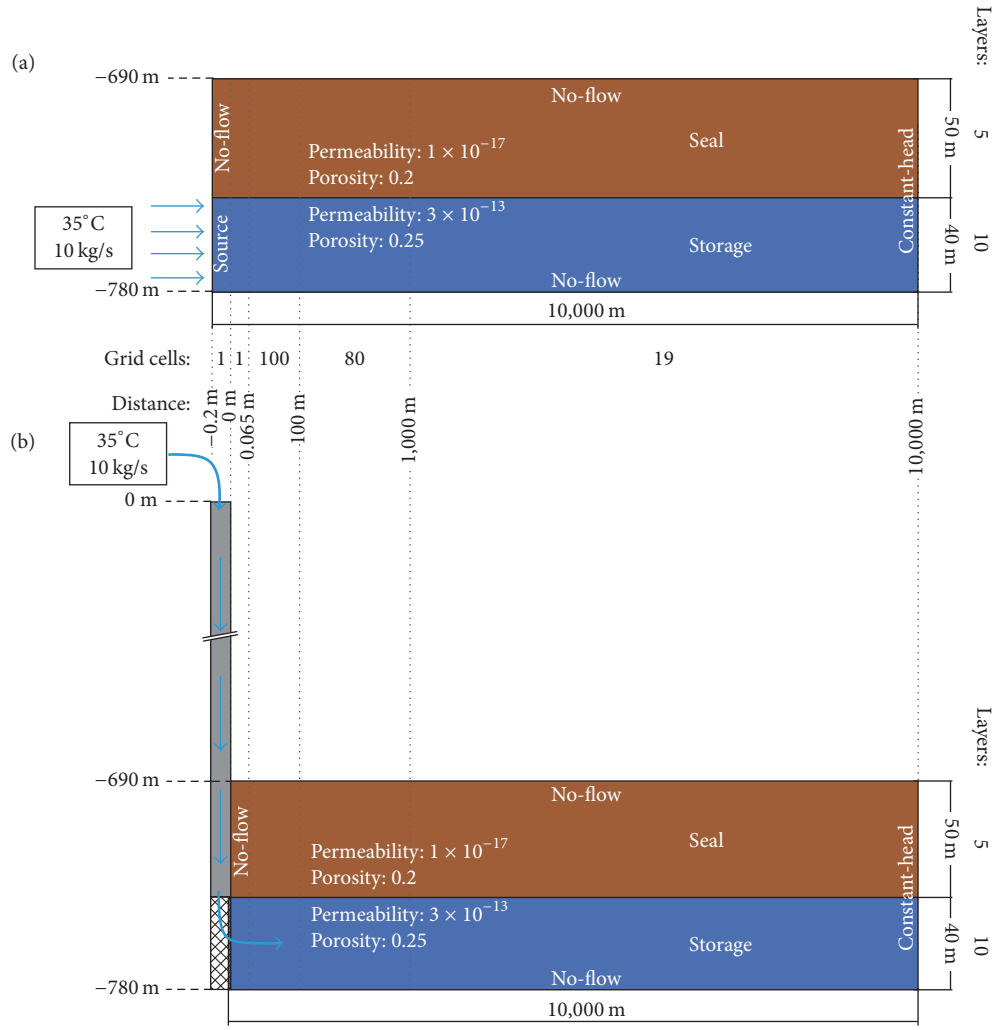

FIGURE 1: Schematic diagrams delineating the 2-dimensional radial models. (a) Case 1 targeted to evaluate the EPM model and (b) Case 2 is for the WR model.

grid-blocks located at the left-most boundary with 1 kg/s injection rate (a total injection rate was 10 kg/s) during 1,095 days (3 years) (Figure 1(a)). The temperature of the injected CO_2 was maintained at 35.0°C, assuming that CO_2 velocity within the wellbore was fast enough to ignore conductive heat transfer from surroundings. Additionally, since there was no wellbore, it was assumed that the Joule Thompson effect was negligible. The ambient temperature based on assigned geothermal gradient was 54.2°C to 55.9°C in the storage formation. In Case 2 (WR model), for simulating CO_2 transport through the wellbore, the wellbore consisting of 84 grid-blocks was added to the left-most boundary from the ground surface to the bottom of target formation (Figure 1(b)). The diameter of the wellbore was set to 0.2 m. From the ground surface to the depth of 690 m (the top of the sealing formation), the 69 grid-blocks with the individual vertical size of 10 m were assigned without coupling to the surrounding formation. However, conductive heat exchange between the wellbore and the surrounding formation was considered by calculating semianalytically [24, 49]. From the depth of 690 m to 780 m, the wellbore consisting of 15 grid-blocks was connected to the storage formation with the same dimension (sealing formation: 5 layers and storage formation: 10 layers). Among 15 grid-blocks, only 10 grid-blocks connected to the storage formation were considered to be the screen interval where CO_2 mass was injected into the storage formation. Dry CO_2 was injected from the well-head where the temperature of injected CO_2 and the injection rate was maintained at 35.0°C and 10 kg/s, respectively. In both models, the relative permeability and capillary pressure were modeled with Corey's curves [50] and van Genuchten function [51], respectively. The mathematical expressions and input parameters for Corey and van Genuchten functions were presented in Table 1.

Finally, in addition to Cases 1 and 2, 6 subcases of Case 2 were developed to evaluate different injection conditions for the WR model (Table 2). Three parameters including the injected CO_2 temperature, the injection rate, and the wellbore diameter were determined to analyze the role of the wellbore process on injected CO_2. Particularly, the injected

Table 1: Parameters and properties used in the basecase model. The definitions of symbols are explained in nomenclature.

Parameters for formation	Values
Permeability	
Storage formation	3×10^{-13} m^2
Sealing formation	1×10^{-17} m^2
Porosity	
Storage formation	0.25
Sealing formation	0.2
Salinity	15%
Surface pressure	1.01×10^5 Pa
Pressure gradient	10,577.8 Pa/m
Surface temperature	20°C
Temperature gradient	0.0461°C/m
Thermal conductivity	2.51 W/m·°C
Parameters for injection	**Values**
Injection rate	10 kg/s
Injection temperature	35°C
Wellbore diameter	0.2 m
Parameters for transport	**Values**
Relative permeability	Corey's model
	$k_{rG} = (1-\overline{S})^2(1-\overline{S}^2)$; $k_{rL} = \overline{S}^4$
	$\overline{S} = (S_L - S_{lr})/(1 - S_{lr} - S_{gr})$
	$S_{lr} = 0.3$, $S_{gr} = 0.05$
Capillary pressure	van Genuchten model
	$P_c = -P_0\left(\left(S^*\right)^{-1/\lambda'} - 1\right)^{(1-\lambda')}$
	$S^* = \left(S_L - S_{lr}\right)/\left(S_{ls} - S_{lr}\right)$
Storage formation	$\lambda' = 0.46$, $S_{lr} = 0.2$, $1/P_0 = 1 \times 10^{-4}$ Pa^{-1}
Sealing formation	$\lambda' = 0.25$, $S_{lr} = 0.2$, $1/P_0 = 1 \times 10^{-5}$ Pa^{-1}

Table 2: Description of sensitivity scenarios.

Case	Injection temperature (°C)	Injection rate (kg/s)	Wellbore diameter (m)
Case 2	35	10	0.2
Case 2-1	45	10	0.2
Case 2-2	60	10	0.2
Case 2-3	35	5	0.2
Case 2-4	35	50	0.2
Case 2-5	35	10	0.13
Case 2-6	35	10	0.05

CO_2 temperatures were selected from relatively high values (35°C–60°C) even though the high injected CO_2 temperature will cause a high energetic cost because of heating up CO_2 [52].

2.2. Numerical Simulator. In this study, two simulators were compared; one for the EPM model applying to Case 1 was TOUGH2/ECO2N [53, 54] and the other for the WR model in Case 2 was T2Well/ECO2N [24, 55]. TOUGH2 is the numerical simulator capable of simulating nonisothermal multiphase and multicomponent fluids in multidimensional porous and fractured media [53]. The ECO2N is a fluid property module that describes the thermophysical properties of H_2O-NaCl-CO_2 system [54, 56]. T2Well/ECO2N, which is the suite of the TOUGH2/ECO2N, is the integrated simulator capable of accounting for both wellbore and storage subdomain where they are controlled by different governing equations [24]. Specifically, the viscous flow within the wellbore was predicted from one-dimensional momentum equation while porous media representing the storage formation were simulated with two-dimensional multiphase version of Darcy's law.

For the specific details regarded to TOUGH2, Pruess et al. [53] can be referred. Here, the governing equations related to T2Well/ECO2N are only explained; the primary governing equations representing mass, energy, and momentum within the wellbore and the storage formation are listed in Table 3. As shown in Table 3, the primary difference between porous medium and the wellbore is consideration of both kinetic ($\mathbf{u}_\beta^2/2$) and potential ($\mathbf{g}z\cos\theta$) energy terms in the energy flux and accumulation equations of the wellbore model. Therefore, while CO_2 migrates through the wellbore, variations in both potential and kinetic energies interactively change the energy state of CO_2 within the wellbore. Additionally, fluid velocities within the wellbore are determined by the mixture velocity (u_m) and the drift velocity (u_d), which is calculated from the Drift-Flux-Model (DFM) [57]. Specifically, u_m is calculated by solving following momentum equation [55]:

$$\frac{\partial}{\partial t}\left(\rho_m u_m\right) + \frac{1}{A}\frac{\partial}{\partial z}\left[A\left(\rho_m u_m^2 + \gamma\right)\right] = -\frac{\partial P}{\partial z} - \frac{\Gamma_w f \rho_m \left|\mathbf{u}_m\right| \mathbf{u}_m}{2A} - \rho_m g\cos\theta, \tag{1}$$

where γ is expressed with the following equation: $\gamma = (S_G/(1-S_G))(\rho_G\rho_L\rho_m/\rho_m^{*2})[(C_0-1)u_m + u_d]^2$, which explains the slip between gas and liquid phases. Subsequently, u_d is calculated with a function of gas saturation (S_G) and other fluid properties:

$$u_d = \frac{\left(1 - C_0 S_G\right) u_c K\left(S_G, K_u, C_0\right) m\left(\theta\right)}{C_0 S_G \sqrt{\rho_G/\rho_L} + 1 - C_0 S_G}. \tag{2}$$

In (2), the characteristic velocity (u_c) indicates the rising velocity of gaseous bubble in a liquid column and $m(\theta)$ denotes the inclination effect of the wellbore. The function for $K(\cdot)$ is used for smooth transition of drift velocity between the bubble rising stage and the film flooding stage. Other terms in (2) can be found in the nomenclature. Further details about the T2Well/ECO2N simulator can be found in Pan et al. [55].

In regard to the salt-precipitation process occurring adjacent to the injection well, a number of previous studies have been conducted with TOUGH2/ECO2N [34, 38–42]. However, only a few studies considered the influence of salinity on both wellbore and reservoir flow [25, 58]. In TOUGH2/ECO2N, the salt-precipitation occurred when water vaporized into dry supercritical CO_2, which was

Table 3: Governing equations utilized in T2Well/ECO2N, which represents fluids through the wellbore and storage formation. The definitions of symbols are explained in nomenclature.

Description	Equation
Conservation of mass and energy	$\frac{d}{dt}\int_{V_n} M^\kappa dV_n = \int_{\Gamma_n} \mathbf{F}^\kappa \cdot \mathbf{n}\, d\mathbf{\Gamma}_n + \int_{V_n} q^\kappa dV_n$
Mass accumulation	$M^\kappa = \phi \sum_\beta S_\beta \rho_\beta X_\beta^\kappa$, for each mass component κ
Mass flux	$\mathbf{F}^\kappa = \sum_\beta \mathbf{u}_\beta \rho_\beta X_\beta^\kappa$, for each mass component κ
Porous medium	
Energy flux	$\mathbf{F}^{NK1} = -\lambda \nabla T + \sum_\beta h_\beta \rho_\beta \mathbf{u}_\beta$
Energy accumulation	$M^{NK1} = (1-\phi)\rho_R C_R T + \phi \sum_\beta \rho_\beta S_\beta \mathbf{u}_\beta$
Darcy velocity	$\mathbf{u}_\beta = -k\frac{k_{r\beta}}{\mu_\beta}(\nabla P_\beta - \rho_\beta \mathbf{g})$ Darcy's Law for each phase β, with $P\beta = PG + Pc$
Wellbore	
Energy flux	$\mathbf{F}^{NK1} = -\lambda \nabla T + \sum_\beta \rho_\beta S_\beta \mathbf{u}_\beta \left(h_\beta + \frac{\mathbf{u}_\beta^2}{2} + \mathbf{g} z \cos\theta \right)$
Energy accumulation	$M^{NK1} = \sum_\beta \rho_\beta S_\beta \left(U_\beta + \frac{\mathbf{u}_\beta^2}{2} + \mathbf{g} z \cos\theta \right)$
Phase velocity	$u_G = C_0 \frac{\rho_m}{\rho_m^*} u_m + \frac{\rho_L}{\rho_m^*} u_d$ Drift-flux model
	$u_L = \frac{(1 - S_G C_0)\rho_m}{(1-S_G)\rho_m^*} u_m - \frac{S_G \rho_G}{(1-S_G)\rho_m^*} u_d$ Drift-flux model

Source: modified after Pan et al. [49].

accounted for the equations of states developed by Spycher and Pruess [32]. The precipitation of salt is able to cause to reduction in both porosity and permeability adjacent to the injection well. In this work, reduction of porosity and permeability due to the salt-precipitation was calculated using a "tubes-in-series" model [53, 59].

$$\frac{k}{k_0} = \theta_s^2 \frac{1 - \Gamma + \Gamma/\omega^2}{1 - \Gamma + \Gamma\left[\theta_s/(\theta_s + \omega - 1)\right]^2} \tag{3}$$

$$\theta_s^2 = \frac{1 - S_S - \phi_r}{1 - \phi_r} \tag{4}$$

$$\omega = 1 - \frac{1/\Gamma}{1/\phi_r - 1}, \tag{5}$$

where k/k_0 denotes the permeability reduction factor. ω is calculated by two independent geometric parameters such as fraction of original porosity ($\phi_r = \phi/\phi_0$) and fractional length of pore body (Γ). According to few previous studies, both ϕ_r and Γ were set to be 0.8 [38, 39].

2.3. Gravity Number. The buoyancy effect is one of the significant factors for determining distribution of both CO_2 plume and associated salt-precipitation [41, 42]. In order to quantitatively assess distribution of salt-precipitation in two cases, the gravity number (N_{gv}) was chosen for evaluating the buoyancy effect on the CO_2 plume in the storage formation. N_{gv} defined below measures the degree of strength of gravity to viscous forces [60]:

$$N_{gv} = \frac{k_v L_s \Delta\rho \mathbf{g}}{H u_i \mu}. \tag{6}$$

where k_v is the vertical permeability, H is the thickness of the storage formation, and L_s, as a characteristic length, is chosen to be equal to the horizontal length of the storage formation. $\Delta\rho$ is the density difference between CO_2 and brine, u_i is the total averaged velocity to the horizontal direction predicted from grid-blocks between wellbore and storage formations, and μ is CO_2 viscosity. In (6), greater N_{gv} indicates dominance of the gravity force on CO_2 plume [61].

3. Comparison of EPM and WR Models (Case 1 versus Case 2)

3.1. Analyses of Wellbore Flow Conditions

3.1.1. Characterization of Multiple Stages in the Wellbore. In Case 1 (EPM model), CO_2 holding constant temperature of 35.0°C was injected into the storage formation (formation pressure from 7.95 MPa to 8.33 MPa) at a constant rate of 10 kg/s throughout the simulation time (Figure 1(a)). Following the injection conditions, CO_2 injected into the storage formation was in supercritical phase consistently preserving its density and viscosity approximately larger than 600 kg/m^3 and 5.0×10^{-5} Pa·s, respectively.

In Case 2 (WR model), CO_2 holding 35.0°C was injected from the well-head at a rate of 10 kg/s (Figure 1(b)). Once CO_2 was entered from the well-head, it transported through the 780 m depth wellbore (Figure 2(a)) while experiencing thermal disequilibrium processes such as heat convection, conduction, frictional effect, and Joule-Thomson effect [21, 27]. Consequently, the temperature of CO_2 reaching the well-bottom was changed from 35.0°C (at the well-head) to approximately 52.0°C. Due to such dynamic disturbance in both temperature and pressure within the wellbore, the thermodynamic properties of CO_2 entering from the well-head were also different with ones reaching the well-bottom.

Figures 2(b)–2(d) showed changes in CO_2 saturation, pressure, and temperature throughout the wellbore during 100 days after CO_2 injection began. According to CO_2 saturation profile in Figure 2(b), three stages were characterized. Stage I (0 to 1.2×10^{-5} day (=1 sec)) defined the status of the wellbore where brine was fully saturated in the well; both pressure and temperature remained hydrostatic and geothermal gradient conditions, initially assigned to the model (Stage I in Figures 2(c) and 2(d)). During Stage II (1.2×10^{-5} day (=1 sec) to 1.2×10^{-2} day (=17.3 min)), the wellbore transited from single (or brine) to multiphase conditions where both brine and CO_2 coexisted; the dynamic interface (dashed purple-line in Figures 2(c) and 2(d)) between injected CO_2 and brine was developed. In addition, the phase transition of CO_2 from gaseous to supercritical phase was observed at a depth of 468 m for the first time (3.2×10^{-3} day), which dynamically evolved with time (Figure 2(b)). Approximately after 3.35 day, gaseous CO_2 in the wellbore completely transited to supercritical phase.

Immediately after CO_2 injection began at Stage II, CO_2 suddenly pushed brine from the well-head, and therefore, increase in CO_2 saturation was observed at the well-head (Figure 2(b)). Due to the encroachment of CO_2 from the well-head, brine positioned at the well-bottom needed to enter the storage formation in which permeability (3×10^{-13} m^2) and capillary pressure were significantly smaller and larger than the wellbore ones, respectively. Because of contrasts in both permeability and capillary pressure between the wellbore and storage formation, the pressure at the wellbore was built up and reached its peak at 2.3×10^{-4} day (Figure 2(c)). Then, subsequent pressure reduction implies that brine at the well-bottom was getting entered the storage formation with continuous CO_2 injection from the well-head. Gradual decrease in the wellbore pressure was observed until the wellbore was completely replaced by CO_2 at 1.2×10^{-2} day (Figure 2(c)).

The temperature profile was somewhat similar to pressure one. At Stage I, temperature ranged from the well-head to well-bottom was 20.0°C to 56.0°C (Figure 2(d)). Then, CO_2 with temperature of 35.0°C was injected from the well-head. While 35.0°C CO_2 displaced the brine from the well-head, relatively warm brine (approximately 50.0–56.0°C) positioned at the bottom of the wellbore entered the storage formation (Stage II). Concurrently, low-temperature brine (20.0°C) was pushed from the well-head to the deeper part of the wellbore by injected CO_2. While the injected CO_2 pushed low-temperature brine downward, diverse thermal processes including thermal convection, conduction, frictional effect, and Joule-Thomson effect occurred concurrently. However, because thermal convection representing the movement of shallow cold-brine toward the well-bottom was more dominant than other thermal effects, overall decrease in temperature was observed in the wellbore.

Immediately after Stage III at 1.2×10^{-2} day, the wellbore was completed replaced by the injected CO_2. Soon, both pressure and temperature increased together (6.9×10^{-2} day). This positive relationship can be attributed to Joule-Thomson effect ($(\partial T/\partial P)_H$), which defines change in temperature during (de)compression of CO_2 based on its counterpart of pressure change under the isenthalpic condition [62]. After 3.35 day, profiles for both pressure and temperature reached the steady-state condition while CO_2 in the wellbore completely became supercritical phase (Figure 2(b)). In summary, due to thermal processes such as frictional effect, heat conduction, and Joule-Thomson effect, temperature of CO_2 which entered the storage formation reached approximately 51-52°C, which was greater than injected CO_2 (35°C) but lower than temperature (54-55°C) of the storage formation.

3.1.2. Variations in Thermophysical Properties of Injected CO_2. Figure 3 showed contours for density, viscosity, specific enthalpy, and Joule-Thomson coefficient of CO_2 dependent on temperature and pressure, which were predicted from Span and Wagner [63]. Figures 3(a) and 3(b) delineated relatively wide ranges covering pressure from 0 to 30 MPa and temperature from 0 to 200°C. Therefore, appropriate ranges for pressure (6 to 10 MPa) and temperature (20 to 80°C) were selected, and CO_2 injection condition was examined for both cases (Figures 3(c) and 3(d)).

The CO_2 injection condition for Case 1 (EPM model; purple symbols) was plotted at 1,095 days (Figure 3(c)). After 1,095 days, pressure from the top to the bottom of the storage formation was changed from 9.16 to 9.26 MPa while maintaining 35°C. At this condition, the injected CO_2 was completely supercritical phase with relatively large density (approximate 650 kg/m^3) and viscosity (approximate 5.2×10^{-5} Pa·s) (Figure 3(c)).

For Case 2 (WR model), 4 profiles were selected; one was at the end of Stage II (1.2×10^{-2} day in Figure 2(b)) immediately after the wellbore was completely filled with CO_2; at this time, the injected CO_2 experienced phase transition from gaseous to supercritical phase at 155 m depth (Point A in Figures 2(b) and 3(c)). Presence of both gaseous and supercritical CO_2 within the wellbore resulted in dynamic (or nonlinear) profile of CO_2. At the well-head, temperature and pressure were 35°C and 6.96 MPa, which was plotted below the critical point (31.1°C and 7.38 MPa) of CO_2. Then, at 155 m (Point A) temperature dropped to 32.6°C ($\Delta T = -2.4$°C) while pressure increased to 7.37 MPa ($\Delta P = +0.4$ MPa). Similar to Han et al. [27] and Lu and Connell [21], decrease in CO_2 temperature occurred in the wellbore due to heat conduction with the surrounding formation; the temperature of the surrounding formation was 27.1°C in this depth. From the ground surface to 155 m, gaseous CO_2 in the wellbore holds

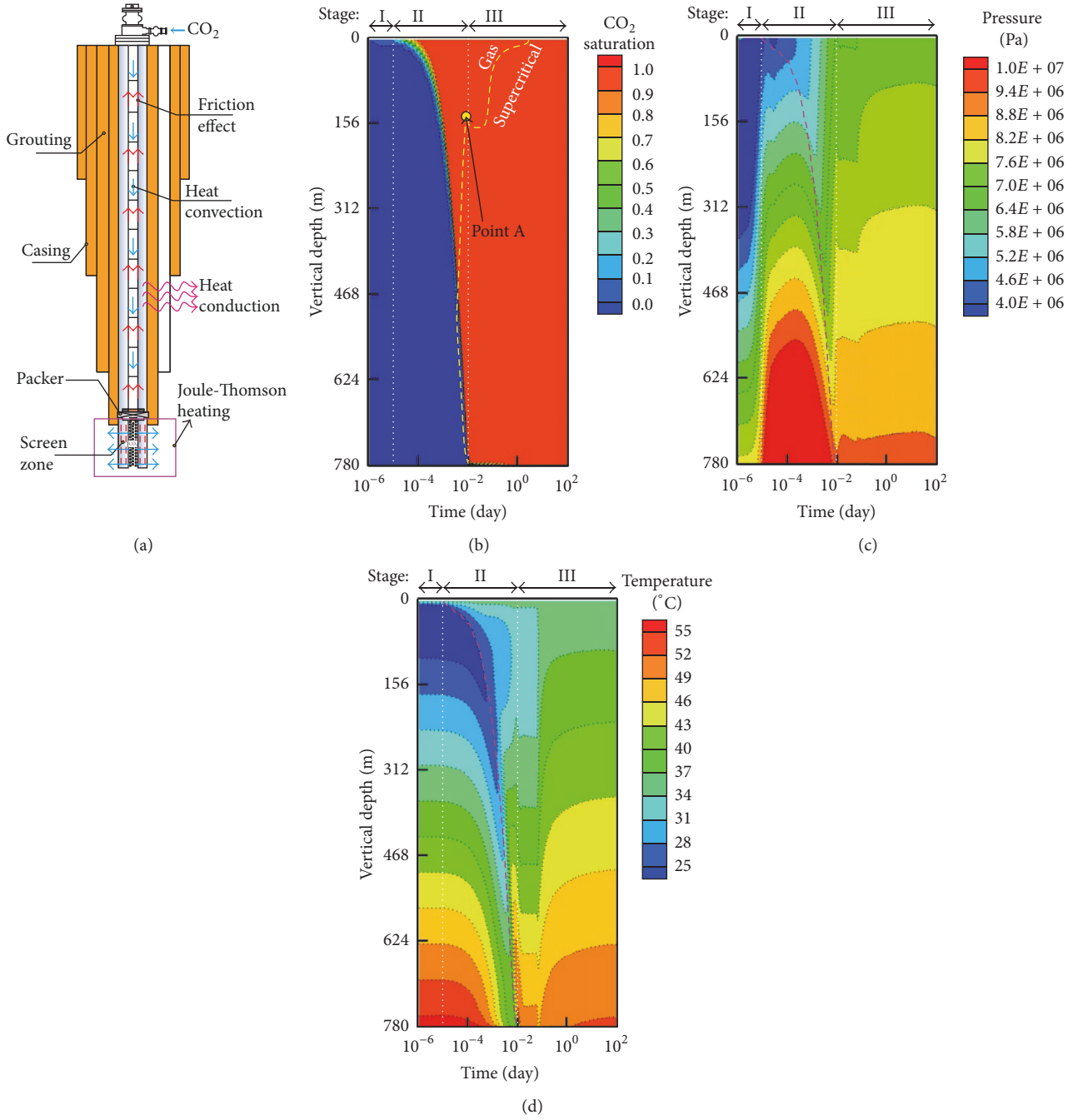

FIGURE 2: Changes in thermophysical properties of CO_2 within the wellbore during 100 days; (a) a schematic diagram delineating CO_2 transport within the wellbore and associated thermal effects; profiles for (b) CO_2 saturation [-], (c) pressure [Pa], and (d) temperature [°C]. The two white dotted lines define the initiation of each different stage while injected CO_2 is displacing the brine in the wellbore (1.2×10^{-5} (=1 sec) and 1.2×10^{-2} (=17.3 min)). The yellow dashed line in (b) represents the interface between gaseous and supercritical CO_2 phase. The purple dashed lines shown in (c) and (d) indicate the dynamic interface between CO_2 and brine.

its density from 219 to 326 kg/m^3, viscosity from 2.0×10^{-5} to 2.3×10^{-5} Pa·s, and Joule-Thomson coefficient decreasing from 9.1 to 8.2°C/MPa. Deeper than 155 m, gaseous CO_2 transited to supercritical phase. Both temperature and pressure increased nonlinearly while deviating from isenthalpic lines (300–350 kJ/kg in Figure 3(d)), implying that supercritical CO_2 in the wellbore did not reach the adiabatic condition yet; thus, various thermal processes including thermal conduction and friction actively affected CO_2 temperature. When CO_2 arrived at the well-bottom, its temperature reached 52.2°C with elevated pressure of 9.5 MPa. Compared to Case 1 (35°C), CO_2 temperature at the well-bottom increased (ΔT=) +17.2°C. Due to significant discrepancy in CO_2 temperature from these two cases, thermodynamic properties of CO_2 were

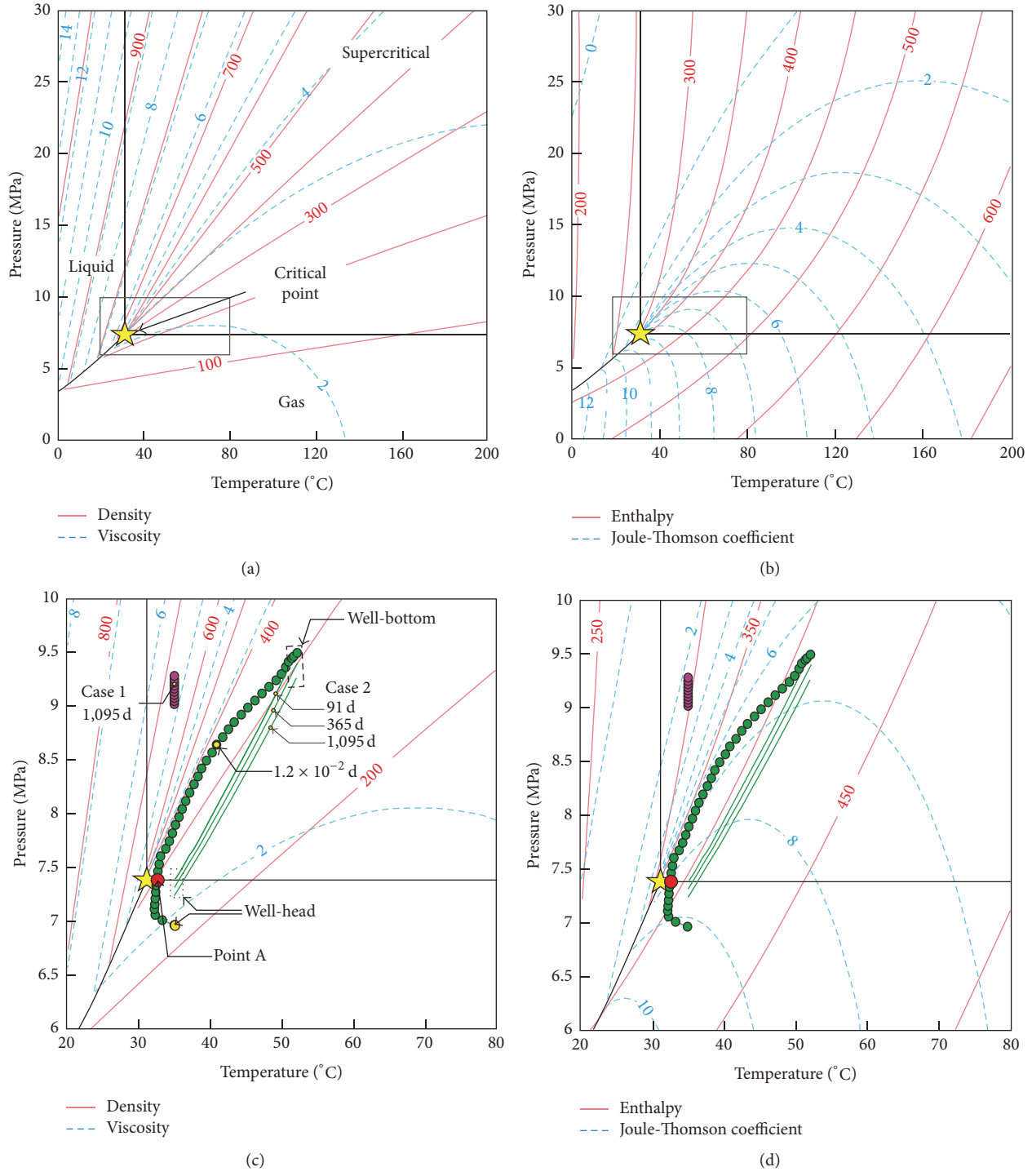

FIGURE 3: Contours of (a) density [kg/m^3] and viscosity [10^{-5} Pa·s] and (b) enthalpy [kJ/kg] and Joule-Thomson coefficient [°C/MPa] in P-T space. Gray box represents a suitable condition for the wellbore during geologic CO_2 sequestration (P: 6 to 10 MPa and T: 20 to 80°C). (c) and (d) represent contours for density, viscosity, enthalpy, and Joule-Thomson coefficient in P-T regime suitable for the wellbore. Purple symbols represent the conditions for CO_2 injection in Case 1. Green symbols and lines represent the conditions for the wellbore in Case 2.

also different which affected the behavior of CO_2 transport in the storage formation.

The other three profiles (91, 365, and 1,095 days) were selected during Stage III. These profiles were paralleled to isenthalpic lines, implying that CO_2 within the wellbore reached the adiabatic condition (Figures 3(c) and 3(d)). In this condition, Joule-Thomson effect on CO_2 temperature would be more significant than any other thermal processes

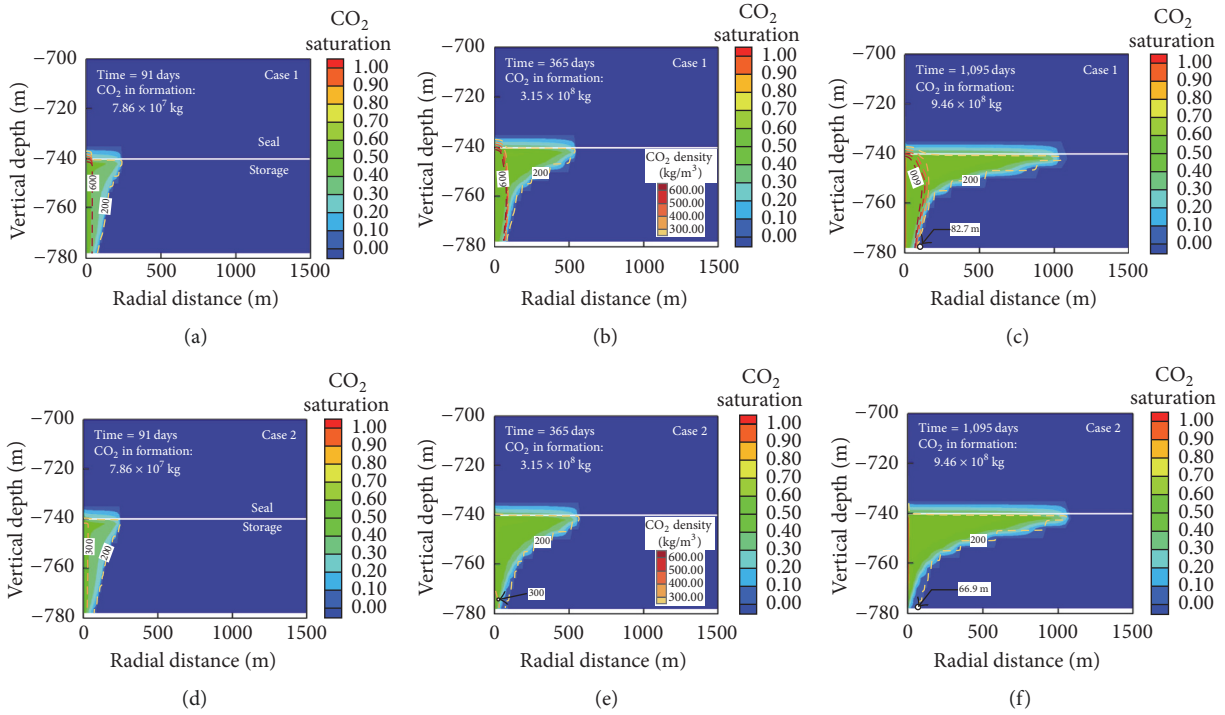

FIGURE 4: Distribution of CO_2 saturation [-] shown as color contours and CO_2 density [kg/m^3] as dashed lines at a series of times (91, 365, 1,095 days). (a), (b), and (c) were simulated from the EPM model (Case 1) while (d), (e), and (f) were from the WR model (Case 2). The isodense lines represent the magnitude of density which follows the legend shown in (b) and (e).

[21]. As seen in Figure 3(d), Joule-Thomson coefficient having positive values decreased from 8.8 to 6.4°C/MPa as approaching to the well-bottom; positive values of Joule-Thomson coefficient imply the adiabatic heating with CO_2 compression, and its effect was relatively large at the shallow depth. All these three profiles revealed that gaseous CO_2 filled the small portion of the well-head even after the arrival of the adiabatic condition. In addition, it is observed that the wellbore pressure slightly decreased with time; the small drop of the well-bottom pressure between 91 and 1,095 days was (ΔP=) −0.2 MPa (9.5 to 9.3 MPa). Correspondingly, CO_2 density and viscosity at the well-bottom were decreased, ($\Delta\rho$=) −19.9 kg/m^3 (311.7 to 291.8 kg/m^3) and ($\Delta\mu$=) -0.1×10^{-5} Pa·s (2.5 to 2.4×10^{-5} Pa·s), respectively (Figure 3(c)).

Overall, when comparing to CO_2 density and viscosity from Case 2 (WR model), Case 1 (EPM model) was 680.0 kg/m^3 and 5.4×10^{-5} Pa·s, respectively, at 1,095 days. As seen, discrepancies in thermophysical properties of CO_2 were significant when two different injection schemes were used even with the same injection rate. This discrepancy became primary reasons for different distribution of CO_2 plume within the storage formation and subsequently the patterns for the salt-precipitation, which will be discussed in following section.

3.2. Analyses of Storage Formation Conditions

3.2.1. Patterns for CO_2 Migration in the Storage Formations. Figure 4 showed the distribution of CO_2 saturation after 91, 365, and 1,095 days of CO_2 injection; Figures 4(a)–4(c) and Figures 4(d)–4(f) were simulated with the EPM model (Case 1) and WR model (Case 2), respectively. Comparing two cases, the same mass of CO_2 was injected into the storage formation (9.46×10^8 kg during 1,095 days), and consequently, CO_2 plume migrated the equal distance of 1,048 m at the interface between the caprock and storage formation (Figures 4(c) and 4(f)). Nevertheless, at the bottom of the storage formation, the frontal location of CO_2 plume was different (82.7 m and 66.9 m for Case 1 and Case 2, resp.), implying that more CO_2 migrated vertically in Case 2, and therefore, more counterflowing brine was developed. According to (6), N_{gv} for each case was calculated and listed in Table 4. As expected, N_{gv} in Case 2 (2.76) was greater than Case 1 (2.20), implying that the buoyancy force acting on the CO_2 plume was greater in Case 2.

In Case 1, density and viscosity of CO_2 in the storage formation were greater than ~600 kg/m^3 (Figures 4(a)–4(c)) and $\sim 5.0 \times 10^{-5}$ Pa·s, respectively (contour lines of CO_2 viscosity were not plotted because they were similar to the isodense lines). However, density and viscosity decreased to ~200 kg/m^3 and $\sim 2.0 \times 10^{-5}$ Pa·s, respectively, while approaching to the margin of the CO_2 plume. In Case 2, CO_2 density was relatively small, showing the range of 200 to 300 kg/m^3 (Figures 4(d)–4(f)); CO_2 density greater than 300 kg/m^3 appeared only next to the injection well until 91 days (Figure 4(d)). In addition, CO_2 viscosity ranged from 2.4×10^{-5} Pa·s adjacent to the wellbore to 2.0×10^{-5} Pa·s at the margin of the CO_2 plume. Differences in CO_2 properties

Table 4: Predicted gravity number for multiple cases as well as associated parameters used in (6).

Case	Time (d)	u_i (m/s)	ρ_{brine} (kg/m^3)	ρ_{CO_2} (kg/m^3)	μ (Pa·s)	N_{gv}
Case 1	91	3.80×10^{-3}	1097.7	557.4	4.5×10^{-5}	2.33
	365	3.84×10^{-3}	1098.1	575.8	4.6×10^{-5}	2.17
	1,095	3.89×10^{-3}	1098.5	571.0	4.5×10^{-5}	2.20
Case 2	91	8.73×10^{-3}	1088.3	294.7	2.4×10^{-5}	2.78
	365	9.03×10^{-3}	1084.7	287.2	2.4×10^{-5}	2.74
	1,095	9.41×10^{-3}	1097.1	277.0	2.3×10^{-5}	2.76
Sensitivity Scenarios						
Case 2-1	1,095	1.09×10^{-2}	1096.5	248.0	2.2×10^{-5}	2.56
Case 2-2	1,095	1.26×10^{-2}	1095.0	223.6	2.2×10^{-5}	2.32
Case 2-3	1,095	5.23×10^{-3}	1097.5	251.4	2.2×10^{-5}	5.36
Case 2-4	1,095	2.49×10^{-2}	1098.1	486.5	3.6×10^{-5}	0.51
Case 2-5	1,095	9.27×10^{-3}	1097.2	280.4	2.3×10^{-5}	2.77
Case 2-6	1,095	4.07×10^{-3}	1098.5	570.7	4.5×10^{-5}	2.12

ρ_{brine}, ρ_{CO_2}, and μ are the average value of brine density, CO_2 density, and CO_2 viscosity in the storage formation, respectively.

such as density and viscosity in these two cases were amplified even after more CO_2 was injected into the storage formation.

3.2.2. Patterns for Salt-Precipitation and CO_2/Brine Flow. At the dry-out zone, different patterns for the salt-precipitation also appeared in these two cases (Figure 5). Here, the "dry-out zone" was defined as a zone where brine had been replaced by injected CO_2, and consequently, its CO_2 saturation approximately reached unity [34]. At the front of the dry-out zone (the interface of dry-CO_2 and brine), pure H_2O is continuously vaporized while remaining the solid salt in the pore. Degree and configuration of precipitated salt were governed by two factors; one was the migration speed of the dry-out front, which was governed by viscous force (e.g., injection rate and horizontal permeability of the storage formation). The others were factors governing buoyancy force (e.g., CO_2 density, the rate for counterflowing brine, and vertical permeability of the storage formation). Additionally, the amount of salt (or salinity) supplied by the counterflowing brine also governed the amount of precipitated salt [37].

In Case 1 (EPM model) following the conventional modeling approach (1 kg/s of CO_2), distribution of horizontal CO_2 flux along the radial distance was almost uniform (e.g., 4.4×10^{-3} kg/(s·m^2) at 9.04 m at 1,095 days) (Figures 5(a) and 5(b)). In contrast, the counterflowing brine with its magnitude of 1.5×10^{-7} kg/(s·m^2) flew opposite to CO_2 flux at 9.04 m (Figure 5(c)). The detailed snap-shots of the growing salt-precipitation were plotted at 91, 365, and 1,095 days in Figures 6(a)–6(c). As seen, the salt was uniformly accumulated throughout the entire thickness of the storage formation with its saturation of approximately 0.04. Correspondingly, the average permeability reduction (k/k_0) calculated from (3) was 65.1% in 1,095 days. Slightly elevated salt saturation appeared at both nearby the wellbore and the interface between sealing and storage formations. Adjacent to the wellbore, the salt saturation increased to be 0.06 due to the complete vaporization of residual brine. At the interface of the sealing formation, the salt saturation was increased due to H_2O vaporization from the inflowing brine. According to Kim et al. [39], residual brine flew from the sealing formation to the dry-out zone where brine was completely displaced by injected dry-CO_2 (Figure 5(c)). Consequently, the maximum salt saturation and the k/k_0 reached 0.078 and 39.2%, respectively.

The WR model (Case 2) was able to predict the profiles for both horizontal and vertical CO_2 mass flow rates within the wellbore (Figure 5(d)). Above the interface (740 m) between the storage and sealing formations, the vertical CO_2 mass flow rate was consistently 10 kg/s because the wellbore was fully cased (red circle in Figure 5(d)). However, once CO_2 entered the screened interval (740 to 780 m), the vertical CO_2 mass flow rate decreased with the depth almost linearly and finally reached zero at the well-bottom. In this interval, the horizontal CO_2 mass flow rate reflected the actual CO_2 injection rate (blue circles in Figure 5(d)). As seen in Figures 5(a) and 5(d), the actual CO_2 injection rates from both cases were different; in Case 2, the actual CO_2 injection rates were larger at the upper storage formation except the interface similar to Vilarrasa et al. [64] and decreased toward the well-bottom. However, throughout the entire thickness, the average actual CO_2 injection rate was the same as the injection rate assigned to Case 1 (i.e., 10 kg/s).

Due to magnitude difference of actual CO_2 injection rates throughout the screen interval, both viscous and buoyancy forces differently acted on CO_2 plume between Case 1 and Case 2 [44]. Furthermore, relatively warm CO_2 (e.g., 52°C) entered from the wellbore to the storage formation also amplified the buoyancy effect on CO_2 plume (Figure 3(c)). Due to these reasons, in Case 2, the injected CO_2 plume rose rapidly, inducing more counterflowing brine flux (5.0×10^{-6} kg/(s·m^2) at 8 m at 1,095 days) along the bottom of the storage formation (Figure 5(f)). Because of

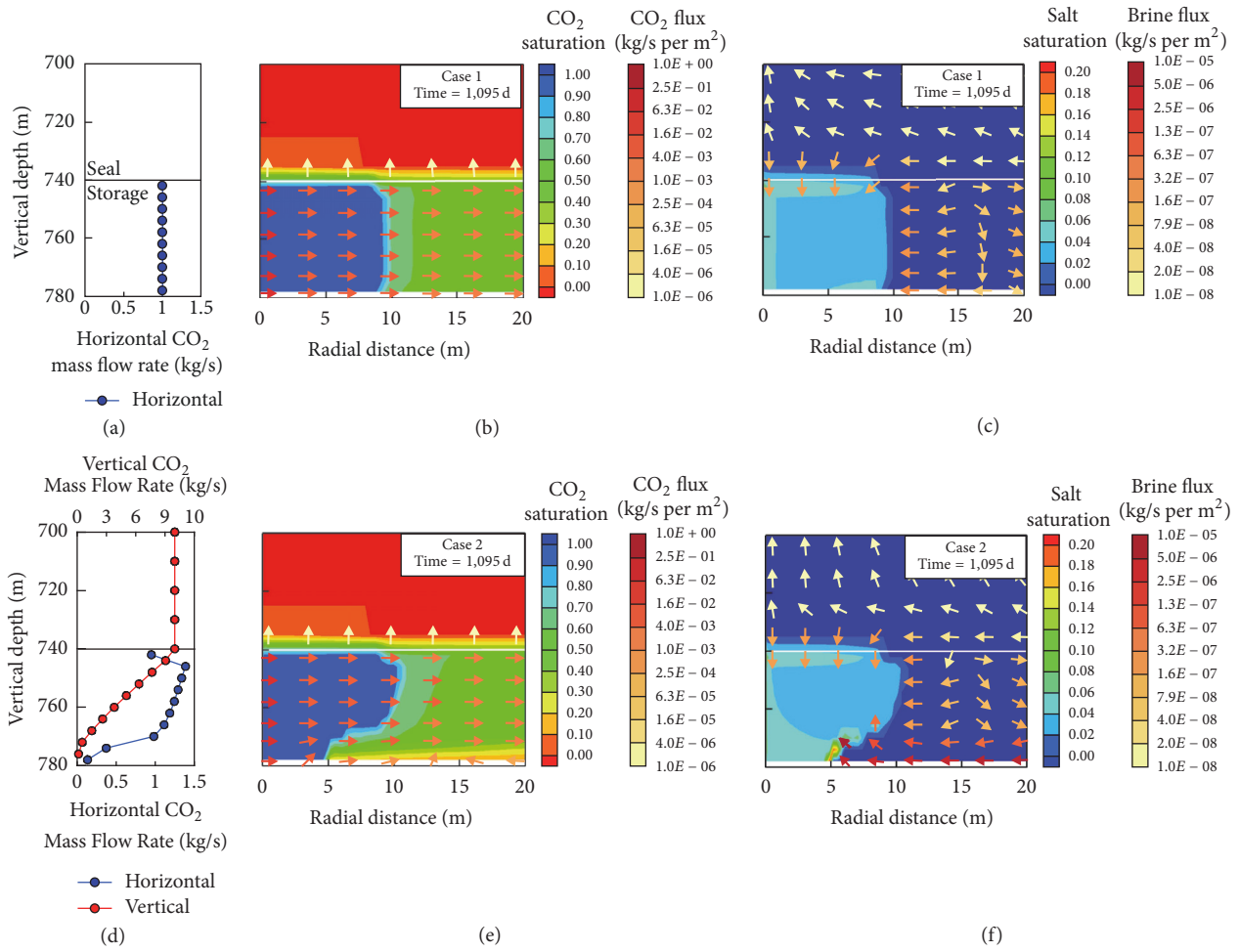

FIGURE 5: Flux patterns for CO_2 and brine near the injection well after the injection of 1,095 days. (a) and (d) predicted CO_2 mass flow rate [kg/s] within grid-blocks representing the wellbore; blue circles are horizontal CO_2 mass flow rate from the wellbore to the storage formation and red symbols are vertical CO_2 mass flow rate within the wellbore. (b) and (e) indicate CO_2 flux [kg/(s·m^2)] with CO_2 saturation. (c) and (f) indicate brine flux [kg/(s·m^2)] with salt saturation. The arrows indicate directions for both CO_2 and brine flux, and the colors represent their magnitude.

strong buoyancy effect on the CO_2 plume, the configuration of the dry-out zone where the salt was precipitated was nonuniform. In particular, the localized salt-peak was developed due to additional supply of salinity by counterflowing brine.

At the zone where the localized salt was precipitated, the maximum salt saturation reached almost equal to porosity (0.25) implying significant deterioration of permeability; the cumulated salt-barrier restricted horizontal propagations of both CO_2 and pressure, consequently reducing effectiveness of the injection well. Figures 6(d)–6(f) showed the development of salt-precipitation at 91, 365, and 1,095 days. According to Figure 6(f), it is distinct that the lower part of the dry-out front stopped expanding after 365 days when the localized salt-peak was developed.

4. Sensitivity Analyses for WR Model

In order to further evaluate the influence of wellbore processes on complete CO_2 injection scenarios and associated salt-precipitation, sensitivity analyses were conducted by varying the injection conditions such as injected CO_2 temperature, injection rate, and wellbore diameter. Then, outputs from developed sensitivity scenarios were compared relative to the base-case representing Case 2 (Table 2).

4.1. Effect of Injected CO_2 Temperature at the Well-Head. Case 2 (35°C), Case 2-1 (45°C), and Case 2-2 (60°C) were designed to evaluate the influence of injected CO_2 temperature while fixing the injection rate of 10 kg/s and the wellbore diameter of 0.2 m. After 1,095 days, CO_2 profiles predicted from three cases became parallel to isenthalpic lines, implying that CO_2, after completely displacing brine within the wellbore, reached the adiabatic condition (Figure 7(a)). While constraining the injection rate, different injected CO_2 temperature resulted in prediction of different well-head pressures ($P_{\text{Case 2}}$ = 7.24 MPa, $P_{\text{Case 2-1}}$ = 7.54 MPa and $P_{\text{Case 2-2}}$ = 7.79 MPa). Nevertheless, the well-bottom pressures were relatively consistent ($P_{\text{Case 2}}$ = 9.26 MPa, $P_{\text{Case 2-1}}$ = 9.29 MPa, $P_{\text{Case 2-2}}$ = 9.30 MPa). Within the wellbore, the hydrostatic pressure

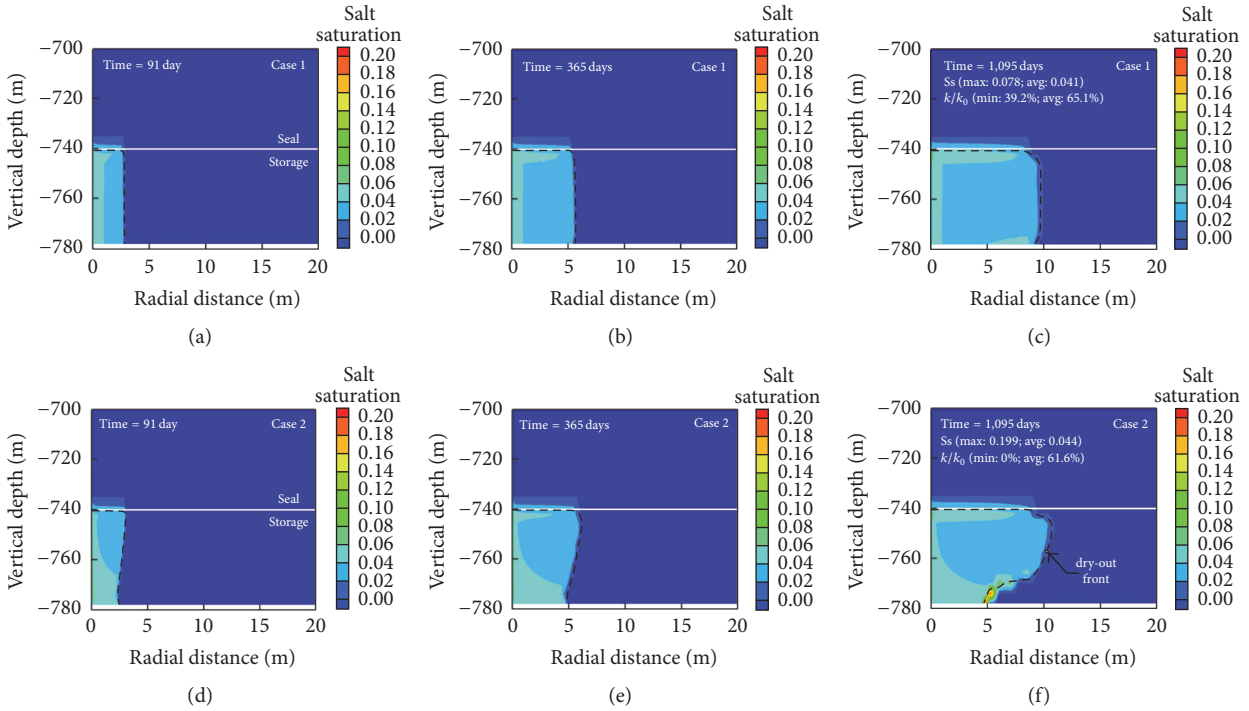

FIGURE 6: Distribution of salt saturation [-] shown as color contours and the dry-out front as dashed lines at a series of times (91, 365, and 1,095 days). (a), (b), and (c) were simulated from the EPM model (Case 1), but (d), (e), and (f) were from the WR model (Case 2).

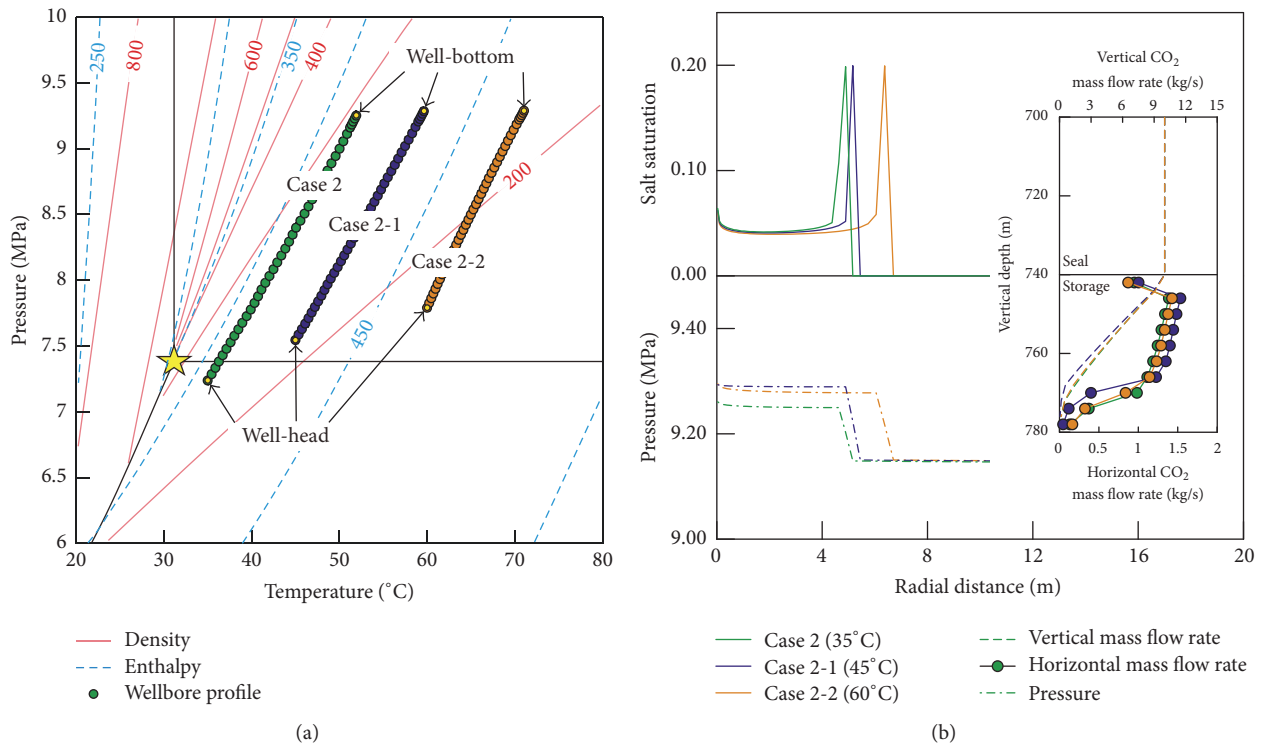

FIGURE 7: (a) Changes of CO_2 properties (density [kg/m^3] and enthalpy [kJ/kg]) within the wellbore and (b) development of salt saturation [-] and built-up pressure [MPa] at the bottom layer. The small figure represents both horizontal and vertical CO_2 mass flow rate [kg/s] within the wellbore at three different injection temperatures (35, 45, and 60°C) after 1,095 days.

(P_{bottom}) at the well-bottom can be expressed to be $P_{\text{bottom}} = P_{\text{head}} + \rho_{CO_2}\mathbf{g}H$. The same injection rate (10 kg/s) indicates that P_{bottom} should be consistent at all cases. However, the magnitude of the second term ($\rho_{CO_2}\mathbf{g}H$) at the right-side varied because ρ_{CO_2} decreased with the increase in injected CO_2 temperature; for example, ρ_{CO_2} at the well-bottom was 291.8 kg/m^3, 251.6 kg/m^3, and 216.8 kg/m^3 in Cases 2, 2-1, and 2-2, respectively. While maintaining the same P_{bottom}, decrease in $\rho_{CO_2}\mathbf{g}H$ resulted in elevated P_{head} as appeared in Figure 7(a). Due to this reason, CO_2 existed as gaseous phase adjacent to the well-head in Case 2, but no more gaseous CO_2 was present as the injected CO_2 temperature was increased.

Within the storage formation, all cases showed the accumulation of localized salt, but the peak was closer to the well as the injected CO_2 temperature decreased (Figure 7(b)); the localized salt-peak was positioned at 4.89 m, 5.16 m, and 6.37 m in Case 2 (35°C), Case 2-1 (45°C), and Case 2-2 (60°C), respectively. Previously, Kim et al. [41] noted that the localized salt-peak was developed closer to the injection well as the buoyancy effect was stronger (or greater N_{gv}, greater temperature). As seen, in our study, calculated N_{gv} of Case 2, Case 2-1, and Case 2-2 was 2.76, 2.56 and 2.32, respectively (Table 4). The relationship between injected CO_2 temperature and N_{gv} was inconsistent with the previous premise defining that less dense (or warm) CO_2 promoted vertical migration more. According to the Mass Flux equation ($F^K = \sum_\beta \mathbf{u}_\beta \rho_\beta X^K_\beta$) shown in Table 3, if CO_2 completely displaced brine adjacent to the wellbore (assuming a single-phase and single-component), the Mass Flux equation can be simplified to be the $\mathbf{F}_{\mathbf{CO_2}} = \mathbf{u}_{CO_2}\rho_{CO_2}$. Here, average horizontal CO_2 mass flow rate ($\mathbf{I_r}$) is expressed to be $\mathbf{I_r} = \mathbf{F}_{\mathbf{CO_2}} \cdot A_i$. In this study, $\mathbf{I_r}$ was 1 kg/s at 10 grid-blocks of the screen interval and the interface area (A_i) of the grid-blocks was fixed to be 2.51 m^2. Correspondingly, $\mathbf{F}_{\mathbf{CO_2}}$ was constant, resulting in the fact that any change in ρ_{CO_2} should accompany variation in $\mathbf{u}_{CO_2}$. For example, in Case 2, Case 2-1, and Case 2-2 increase in the injected CO_2 temperature accompanied the decrease in ρ_{CO_2}, which resulted in elevated $\mathbf{u}_{CO_2}$ within the storage formation.

Subsequently, in (6), increase in $\mathbf{u}_{CO_2}$, which was included in the denominator, decreased N_{gv} even if $\Delta\rho$ increased due to increasing the injected CO_2 temperature. Due to this complicated relation, increase in injected CO_2 temperature ultimately decreased the buoyancy effect on CO_2 plume while enhancing viscous force (or enhancing $\mathbf{u}_{CO_2}$). Additionally, the magnitude of the salt-peak (solid-line) was similar in all cases (approximately 0.19), implying that different CO_2 temperature did not cause to variation in the size of the salt-peak. Nevertheless, the location of the salt-peak was different and also coincident to the realm where the pressure (dot-dashed) was built up, implying that the salt-peak served as a local barrier which prevented the propagation of pressure pulse to the far-region.

4.2. Effect of Injection Rate. The effect of injection rate on the wellbore process and associated salt-precipitation was investigated throughout Case 2-3 (5 kg/s), Case 2 (10 kg/s), and Case 2-4 (50 kg/s) (Table 2). After 1,095 days, CO_2 profiles in all cases reached the adiabatic condition (Figure 8(a)). At the well-head, greater injection rate pushing more CO_2 to the well-bottom induced larger well-head pressure ($P_{\text{Case 2-3}}$ = 7.10 MPa, $P_{\text{Case 2}}$ = 7.24 MPa, and $P_{\text{Case 2-4}}$ = 8.06 MPa). Likewise, the well-bottom pressure was elevated ($P_{\text{Case 2-3}}$ = 9.03 MPa, $P_{\text{Case 2}}$ = 9.26 MPa, and $P_{\text{Case 2-4}}$ = 11.63 MPa).

Under the adiabatic condition, change in pressure accompanied variation of temperature. For example, CO_2 profile in Case 2-4 (50 kg/s) approximately lied along ~5°C/MPa contour line for Joule-Thomson coefficient shown in Figure 3(d). Considering that such a high injection rate minimized thermal exchange between CO_2 within the wellbore and the surrounding formation, pressure difference ($\Delta P_{\text{Case 2-4}}$ = 11.63 − 8.06 = 3.57 MPa) between the well-bottom and well-head resulted in change of temperature $\Delta T_{\text{Case 2-4}}$ = ~5°C/MPa × 3.57 MPa = ~17.85°C), which was similar to the model-predicted temperature difference ($\Delta T_{\text{Case 2-4}}$ = 17°C) between the well-bottom (52°C) and well-head (35°C) (Figure 8(a)). For Cases 2-3 (5 kg/s) and 2 (10 kg/s), CO_2 profiles for relatively small injection rates fell on large Joule-Thomson coefficient (8.7~7.3°C/MPa) shown in Figure 3(d). By applying the same principle, it can be concluded that the wellbore dynamic model reasonably proved temperature disturbance on CO_2 under the adiabatic condition.

Within the storage formation, the salt-peak only occurred when the injection rate was small (Cases 2-3 and 2 in Figure 8(b)). In particular, the smaller injection rate caused to the development of the salt-peak closer from the wellbore. For example, in Case 2-3, the localized salt-precipitation was developed at 0.65 m from the injection well by surrounding the half of the screen interval (from the well-bottom to 760 m). Similarly, in the magnified figure of Figure 8(a), CO_2 profile in Case 2-3 was not linear at the well-bottom; the slope of CO_2 profile was different from 760 to 780 m due to the development of salt-barrier. Because the salt-barrier was developed immediately next to the wellbore, the horizontal CO_2 mass flow rate became almost zero (blue circles in the small figure of Figure 8(b)). Without CO_2 entering the storage formation, the built-up pressure was small (ΔP = 0.5 MPa; from 8.3 MPa to 8.8 MPa) (blue dot-dashed line in Figure 8(b)). This negligible change in pressure within the storage formation implies that the developed salt-barrier effectively segregated the pressure propagation from the wellbore to the storage formation.

In high injection rate (Case 2-4, 50 kg), the elevated viscous force minimized the development of the salt-peak. Therefore, the salt-accumulation horizontally extended to 27.1 m while developing the uniform salt saturation of 0.03 (Figure 8(b)). The pressure in the storage formation increased due to high injection rate but decreased logarithmically from the wellbore. In the wellbore, vertical CO_2 mass flow rate decreased linearly from 740 m to the well-bottom (orange dashed line in the small figure of Figure 8(b)). Meanwhile, the horizontal CO_2 mass flow rate was 5 kg/s in each grid-block except at the interface of the seal and the well-bottom. Finally, the calculated N_{gv} of Case 2-3 where the dry-out front was only extended to 0.65 m was the largest (5.36), but the N_{gv} of Case 2-4 was only 0.51 with the extended dry-out front to be 27.10 m (Table 4).

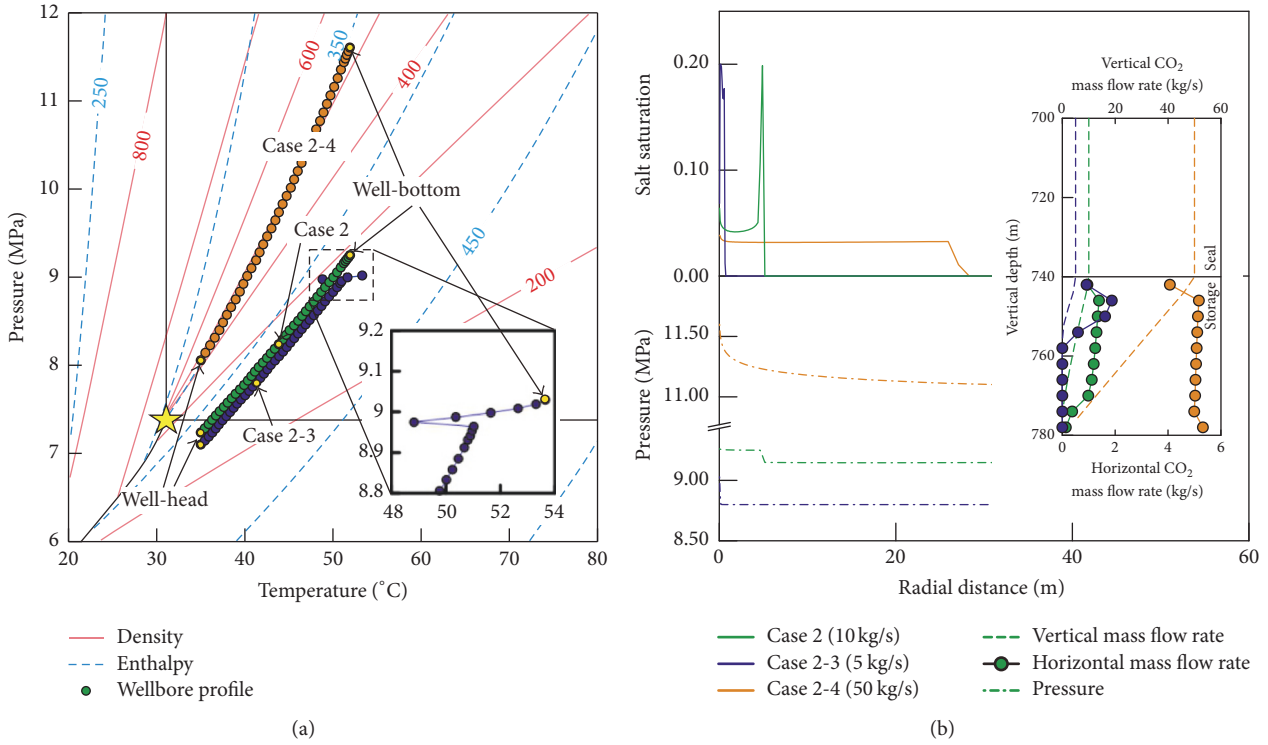

FIGURE 8: (a) Changes of CO_2 properties (density [kg/m^3] and enthalpy [kJ/kg]) within the wellbore and (b) development of salt saturation [-] and built-up pressure [MPa] at the bottom layer. The small panel represents both horizontal and vertical CO_2 mass flow rate [kg/s] within the wellbore at three different injection rates (5, 10, and 50 kg/s) after 1,095 days.

4.3. Effect of Wellbore Diameter. In this study, after fixing the injected CO_2 temperature (35°C) and rate (10 kg/s), the wellbore diameter was varied at Case 2-6 (0.05 m), Case 2-5 (0.13 m), and Case 2 (0.2 m) (Table 2). As shown in Figure 9(a), CO_2 profiles of both Case 2 and Case 2-5 were almost parallel to isenthalpic lines, indicating the arrival of the adiabatic condition. CO_2 profile of Case 2-5 was slightly shifted from Case 2; discrepancies were $\Delta P_{\text{well-head}}$ = 0.06 MPa, $\Delta P_{\text{well-bottom}}$ = 0.01 MPa, and $\Delta T_{\text{well-bottom}}$ = 0.52°C, respectively. Similarly, magnitudes of vertical and horizontal CO_2 mass flow rates were nearly the same, and thus, both configuration of the precipitated salt-barrier and built-up pressure were almost equivalent (Figure 9(b)). N_{gv} for Case 2 and Case 2-5 also showed similar values, 2.76 and 2.77, respectively (Table 4).

When the wellbore diameter decreased furthermore to 0.05 m (Case 2-6), CO_2 profile was changed significantly (Figure 9(a)). First of all, the pressure profile was overturned. Previously, both Case 2 and Case 2-5 revealed that the wellbore pressure was elevated with increase in depth, and thus, the well-bottom pressure was the highest. However, in Case 2-6, the well-head pressure was the highest one (9.9 MPa after 1,095 days), and the pressure decreased along the depth, reaching to 9.1 MPa adjacent to the interface (746 m depth) (the magnified figure in Figure 9(a)). Below 746 m, the pressure overturned with increasing both (ΔP=) 0.2 MPa and (ΔT=) 0.4°C to the well-bottom. In order to understand pressure overturn within the wellbore, it is important to understand the relationship between gravitation and frictional forces.

While CO_2 migrates through the wellbore, both gravity and frictional forces must leverage each other. Here, the gravitational force can be calculated from $\mathbf{F}_g = \rho_{CO_2} V_{CO_2} \mathbf{g}$; V_{CO_2} is CO_2 volume. The frictional force ($\mathbf{F}_f = \boldsymbol{\tau}_w \Gamma_w l_w$) can be obtained by multiplying the shear stress ($\boldsymbol{\tau}_w$) to the perimeter of wellbore ($\Gamma_w = \pi d$, d is the wellbore diameter) and the wellbore length (l_w). Considering that the wellbore is completely filled with CO_2 after 1,095 days, the shear stress ($\boldsymbol{\tau}_w$) can be calculated with the following equation [55]:

$$\boldsymbol{\tau}_w = \frac{1}{2} f \rho_{CO_2} \left|\mathbf{u}_{CO_2}\right| \mathbf{u}_{CO_2}. \tag{7}$$

Here, the friction coefficient (f) is dependent on the Reynolds number ($\text{Re} = \rho_{CO_2} u_{CO_2} d/\mu_{CO_2}$) within the wellbore. Then, $\mathbf{F}_f$ can be expressed as

$$\mathbf{F}_f = \boldsymbol{\tau}_w \Gamma_w l_w = \frac{1}{2} f \rho_{CO_2} \left|\mathbf{u}_{CO_2}\right| \mathbf{u}_{CO_2} \Gamma_w l_w. \tag{8}$$

As described before, the vertical mass flow rate is $\mathbf{I_r} = \mathbf{F_{CO_2}} \cdot A = \rho_{CO_2} \mathbf{u_{CO_2}} \pi (d/2)^2$. Subsequently, $\mathbf{I_r}$ can be rearranged by replacing $\mathbf{u}_{CO_2}$ in $\mathbf{F}_f$ shown in

$$\mathbf{F}_f = 8 f \frac{\mathbf{I}_r^2}{\rho_{CO_2} \pi d^3} l_w. \tag{9}$$

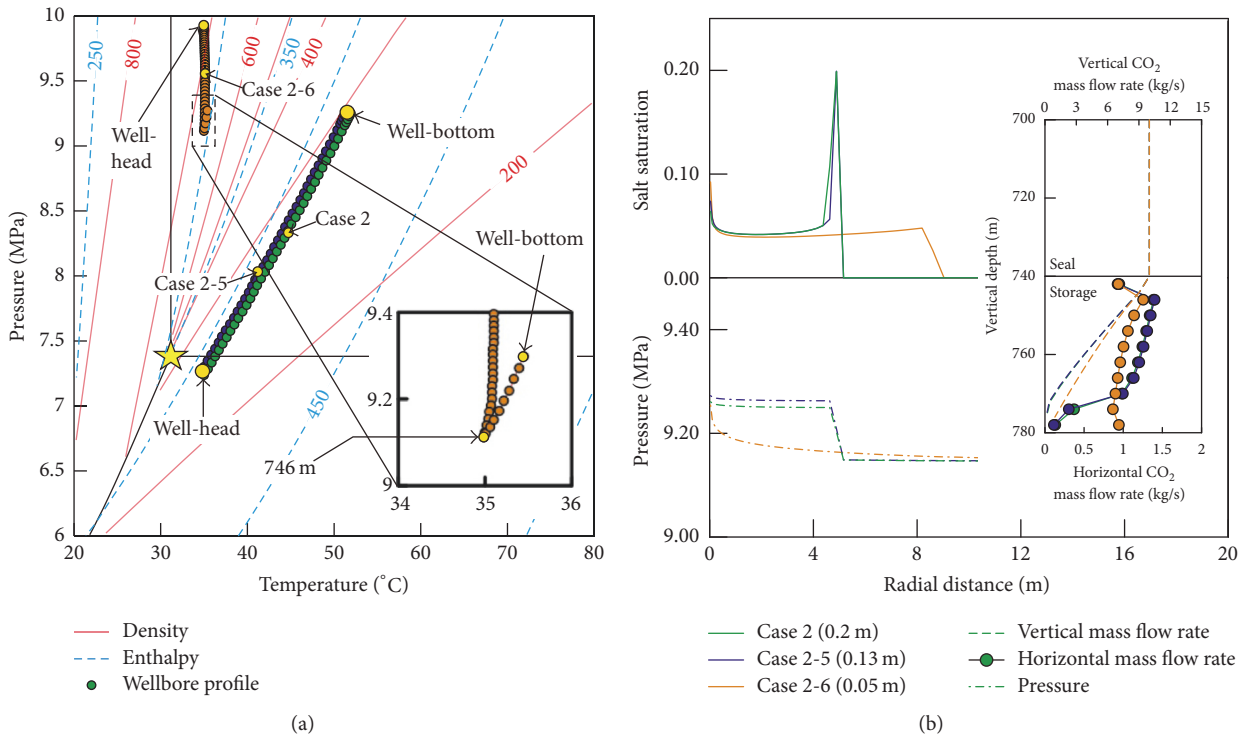

FIGURE 9: (a) Changes of CO_2 properties (density [kg/m^3] and enthalpy [kJ/kg]) within the wellbore and (b) development of salt saturation [-] and built-up pressure [MPa] at the bottom layer. The small figure represents both horizontal and vertical CO_2 mass flow rate [kg/s] within the wellbore with three different wellbore diameters (0.05, 0.13, and 0.2 m) after 1,095 days.

When the CO_2 injection rate was constant at the well-head, the vertical CO_2 mass flow rate ($\mathbf{I_r}$) was also invariable from the well-head to the interface (the orange dashed line in the small figure of Figure 9(b)). At constant $\mathbf{I_r}$, (9) represents the fact that $\mathbf{F}_f$ is dependent on friction coefficient (f), CO_2 density (ρ_{CO_2}), and wellbore diameter (d) and length (l_w). In particular, the third power of wellbore diameter (d^3) in (9) indicates that the wellbore diameter can influence $\mathbf{F}_f$ more than any other parameters. For example, when the wellbore diameter was decreased 4 times from 0.2 m (Case 2) to 0.05 m (Case 2-6), the average $\mathbf{F}_f$ per unit depth between the well-head and 746 m increased from 0.5 N/m to 16.0 N/m (32 times). However, the average $\mathbf{F_g}$ per unit depth decreased from 82.2 N/m to 13.8 N/m (approximately 6 times). As seen, when the wellbore diameter was sufficiently small (e.g., 0.05 m), $\mathbf{F}_f$ was large enough to exceed $\mathbf{F_g}$, which induced the overturn of the pressure profile.

Within the wellbore, the pressure relationship between two grid-blocks next to each other can be written as $P_2A = P_1A + \mathbf{F}_g - \mathbf{F}_f$. Here, P_1 is the pressure of the grid-block 1 positioning above the grid-block 2, and A is the cross-section area between two grid-blocks. When $\mathbf{F}_f$ was greater than $\mathbf{F}_g$ ($\mathbf{F}_f > \mathbf{F}_g$), P_1 should be greater than P_2 ($P_1 > P_2$), indicating that the well-head pressure was the largest along the wellbore and decreased with the depth, as seen in Case 2-6. The similar pressure profile along the wellbore was also observed by Pan et al. [24] who simulated the wellbore processes at a 100 kg/s injection rate.

Interestingly, at Case 2-6 (0.05 m), pressure was increased again with the depth below 746 m (the magnified figure in Figure 9(a)). It can be attributed to decrease in vertical CO_2 mass flow rate ($\mathbf{I_r}$) at the screen interval where horizontal CO_2 mass flow rate increased (the orange circle in the small figure of Figure 9(b)). Decrease in $\mathbf{I_r}$ induced a decrease in $\mathbf{F}_f$ as seen in (9). Therefore, at the screen interval, $\mathbf{F_g}$ overcame $\mathbf{F}_f$ in turn; for example, from 746 m to the well-bottom average $\mathbf{F_g}$ and $\mathbf{F}_f$ per unit depth were 13.3 N/m and 3.9 N/m, respectively.

In additional to the pressure profile, the temperature profile along the wellbore was also perturbed due to the variation in the wellbore diameter. Different from Cases 2 and 2-5, CO_2 profile in Case 2-6 was not situated at the isenthalpic condition; from the well-head to 746 m, temperature change was negligible ($\Delta T = 0^\circ$C), and from 746 m to the well-bottom CO_2 temperature was slightly increased ($\Delta T = 0.4^\circ$C) (the magnified figure in Figure 9(a)). From the well-head to 746 m, no change in CO_2 temperature indicates that CO_2 in the wellbore did not experience major thermal disturbances due large vertical CO_2 velocity. However, below 746 m, decrease in $\mathbf{I_r}$ accompanied the reduction of $\mathbf{u}_{CO_2}$, resulting to slight enhancement of thermal conduction between storage formation and the wellbore. Nevertheless, due to lack of thermal perturbation in Case 2-6, temperature of CO_2 entering the storage formation was almost the same to one for Case 1 (EPM model) (Figures 3(c) and 9(a)). Thermophysical properties of CO_2 entering the storage formation were similar

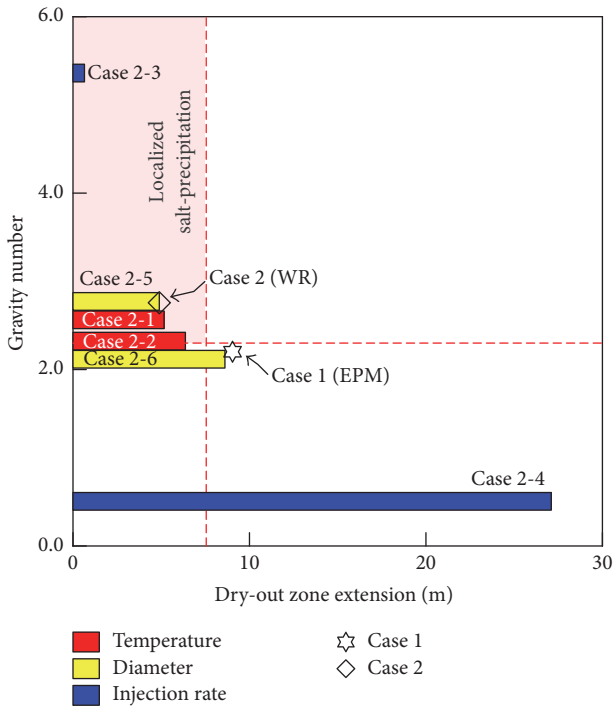

FIGURE 10: Relationship delineating between gravity number and the location of dry-out front after 1,095 days. The red box indicates the area developing the localized salt-precipitation.

to each other. As shown in Figure 9(b), the dry-out front expanded to similar distance (8.61 m) to Case 1 where the dry-out front expanded to 9.04 m without developing the localized salt-precipitation (Figure 5(c)). The calculate N_{gv} was also similar to each other (Case 2-6: 2.12 and Case 1: 2.20), which implies that the injection condition from the small diameter wellbore could mimic one for Case 1 (EPM model) under the specific conditions.

4.4. Gravity Number versus Dry-Out Front. Development of salt-barrier and its extent from the wellbore were governed by dominance between buoyancy and viscous forces, which was estimated from gravity number (N_{gv}) (Table 4). Interestingly, N_{gv} revealed the negative relationship with the extension of the dry-out front (Figure 10); the threshold of the N_{gv} developing the localized salt-barrier was approximately 2.3. At that time, the extent of localized salt-barrier was less than 8 m from the injection well. In Case 1 (the EPM model), the 10 grid-blocks imitated the wellbore where CO_2 flow was solved with Darcy's law (Figure 1(a)). Here, the salt saturation uniformly extended to 9.04 m from the wellbore without developing the localized salt-precipitation (the star symbol in Figure 10). Whereas in Case 2 (diamond symbol) adopting the WR model, N_{gv} increased while developing the localized salt-barrier, and the dry-out front became smaller than 4.89 m.

For the sensitivity study of the wellbore diameter, both predicted N_{gv} and dry-out extent were almost the same in both Case 2 (0.2 m) and Case 2-5 (0.13 m). However, when the wellbore diameter decreased further to 0.05 m (Case 2-6), the viscous force became dominant in the storage formation. Consequently, the salt was precipitated uniformly to 8.61 m. Indeed, the 0.05 m diameter wellbore behaved similarly to Case 1 (EPM model). Effect of the injected CO_2 temperature was minimal (Case 2, Case 2-1, and Case 2-2) (Figure 10). While the temperature of injected CO_2 increased, CO_2 density was decreased, which resulted in elevated CO_2 velocity ($\mathbf{u}_{CO_2}$) within the storage formation (see discussion in Section 4.1). Due to the elevated $\mathbf{u}_{CO_2}$, viscous force became dominant, and thus, the dry-out front was extended further (Case 2-1: 5.16 m and Case 2-2: 6.37 m).

Finally, sensitivity analysis with the injection rate (Case 2-3, Case 2, and Case 2-4) revealed that the injection rate plays a significant role in the dry-out zone extent and development of the localized salt-precipitation (Figure 10). When the injection rate decreased to the 5 kg/s, the localized salt-barrier was developed immediately adjacent to wellbore (0.65 m). Consequently, the salt-barrier prevented the CO_2 entering the storage formation. On the contrary, the large injection rate (50 kg/s) significantly enhanced viscous force of CO_2 plume in the storage and extended the dry-out front to the furthest distance (27.10 m) in all cases without the development of localized salt-precipitation.

5. Discussion

The numerical studies varying multiple CO_2 injection scenarios were conducted to elaborate the relationship between the wellbore process and associated changes occurred within the storage formation. Due to the complex involving wellbore flow and the salt-precipitation, the dynamic changes of CO_2 properties and wellbore conditions were necessary to be evaluated. Here, the transient, coupled wellbore-reservoir model aided to simulate the CO_2 flow more precisely than conventional EPM model for various injection scenarios in geologic CO_2 sequestration. For example, migration patterns of CO_2 plume, which was governed by thermodynamic properties of CO_2, could affect the storage capacity and possibly leakage potentials [65]. The resulting development of the localized salt-barrier was able to significantly influence the injectivity [40, 41].

In the simulation studies, a few limitations were included. The injected CO_2 temperature at the well-head was chosen to be higher than the critical temperature. Therefore, the injected CO_2 from the well-head was always to be supercritical state. However, in the field implementation, the high CO_2 temperature implies high energetic cost requiring for heating up CO_2 [52]. Therefore, for the consideration of economically optimum CCS operations, the injection of gaseous CO_2 should be evaluated using the wellbore dynamic model too. In addition, dependent on conditions of the storage formation, the rate of conductive heat transfer between CO_2 plume and formation fluid would be different as well as the magnitude of salt-precipitation [66]. In this work, assigned temperature and pressure gradients in the model were greater than ones for typical sedimentary basins. In particular, conditions for the storage formation such as temperature, pressure gradients, and the injection depth were referred from the first pilot-scale CO_2 injection

project at Yeong-il embayment in Korea, which is located close to the tectonically active region in Japan [67]. Due to consideration of relatively warm and pressurized storage formation, CO_2 plume behavior within both the wellbore and the storage formation could be different from CO_2 injected in conventional sedimentary basins. Finally, even if this study did not consider, properties of the storage formation involving permeability, porosity, heterogeneity, burial depth, and lithology of the storage formation could influence CO_2 flux entering from the wellbore to the storage formation and resulting salt-precipitation. Nevertheless, such effects were not considered here, but they are equally important to be evaluated.

6. Conclusions

The WR model (Case 2) was selected to simulate fluid flows in both the wellbore and the storage formation. Additionally, the EPM model (Case 1) was compared to the WR model (Case 2) for evaluating any discrepancies (Figure 1). After considering the wellbore flow process, entering CO_2 mass flow rate, CO_2 phase, and thermodynamic properties at the screen interval can be predicted more accurately. Consequently, the patterns of CO_2 plume and salt-precipitation at the storage formation showed different distribution between two cases. The precipitated salt in Case 2 served as a barrier to prevent horizontal propagation of CO_2 plume from the injection well and also deteriorate the injectivity. Then, the transient, coupled wellbore-reservoir model can simulate the CO_2 flow more precisely than conventional EPM model for various injection scenarios in GCS. Additionally, under the different injection conditions (injected CO_2 temperature, injection rate, and wellbore diameter) the simulation results, such as pressure build-up, CO_2 migration, and patterns of salt-precipitation, showed various values. Therefore, through a series of multiple simulations, it can be concluded that the wellbore flow processes can play an important role in the CO_2 injection scenarios and significantly influence the changes which occurred by CO_2 injection in the storage formation. The dynamic changes of CO_2 properties and wellbore conditions are necessary for modeling the CO_2 migration and development of salt-precipitation at the storage formation. For example, patterns of CO_2 plume, which was determined by thermodynamic properties of CO_2, can particularly affect the storage capacity and possibly leakage potentials. In addition, development of the localized salt-barrier can significantly influence the injectivity. Therefore, this study not only deepens understanding of wellbore flow process but also can provide theoretical support for the commercial-scale of CO_2 injection projects.

Nomenclature

A: Cross-sectional area, m^2
C_0: Shape factor
C_R: Heat capacity of the rock, J/kg·K
$\mathbf{g}$: Acceleration of gravity vector, m/s^2
f: The fanning friction coefficient, dimensionless
$\mathbf{F}$: Mass or energy flux vector, $kg/m^2{\cdot}s$ or W/m^2
h: Specific enthalpy, J/kg
k: Permeability, m^2
k_0: Initial permeability, m^2
k_r: Relative permeability, m^2
K_u: Kutateladze number
M: Mass accumulation term, kg/m^3
$\mathbf{n}$: Outward unit normal vector
P: Pressure, Pa
P_0: The strength coefficient
P_c: Capillary pressure, Pa
q: Mass or heat source term, $kg/m^3{\cdot}s$ or W/m^3
S: Saturation
S_{gr}: Supercritical-phase CO_2 residual saturation
S_{lr}: Brine residual saturation
S_{ls}: Saturated brine saturation
t: Time, s
T: Temperature, °C
$\mathbf{u}$: Velocity, m/s
U: Internal energy, J/kg
V_n: Volume, m^3
X: Mass fraction
z: Z-coordinate (positive upward), m.

Greek Letters

Γ: The fractional length of the pore bodies, m
Γ_n: Area of closed surface, m^2
Γ_w: The perimeter of the well cross-section, m
θ: Angle between wellbore and vertical direction, °
λ: Thermal conductivity, W/°C·m
λ': The parameter depending on pore geometry
μ: Dynamic viscosity, kg/m·s
ρ: Density, kg/m^3
ρ_m^*: Profile-adjusted average density, kg/m^3
ρ_m: The density of the gas-liquid mixture, kg/m^3
ϕ: Porosity
ϕ_r: The fraction of original porosity at which permeability is reduced to zero
ϕ_0: Initial Porosity.

Subscripts and Superscripts

β: Phase index
d: Drift
G: Gas
κ: Component index
L: Liquid
m: Mixture
$NK1$: Energy component

R: Rock
$r\beta$: Relative for phase β
S: Solid.

Conflicts of Interest

The authors declare that there are no conflicts of interest regarding the publication of this paper.

Acknowledgments

This research was partially supported by Demonstration-Scale Offshore CO_2 Storage Project in Pohang, Basin, Republic of Korea, funded from Energy Efficiency & Resources of the Korea Institute of Energy Technology Evaluation and Planning (KETEP) which was granted financial resource from the Ministry of Trade, Industry & Energy, Republic of Korea (no. 20162010201980) and also supported by Basic Science Research Program through the National Research Foundation of Korea (NRF) funded by the Ministry of Education (no. 2016R1D1A1B01008715). The authors also acknowledge financial support by the Basic Research Project of the Korea Institute of Geoscience and Mineral Resources (KIGAM) funded by the Ministry of Science and ICT.

References

[1] IPCC, *Special Report on Carbon Dioxide Capture and Storage*, Cambridge University Press, Cambridge, U.K, 2005.

[2] H. Audus, "Greenhouse gas mitigation technology: An overview of the CO_2 capture and sequestration studies and further activities of the IEA greenhouse gas R&D programme," *Energy*, vol. 22, no. 2-3, pp. 217–221, 1997.

[3] S. Bachu, "CO_2 storage in geological media: role, means, status and barriers to deployment," *Progress in Energy and Combustion Science*, vol. 34, no. 2, pp. 254–273, 2008.

[4] J. T. Birkholzer, C. M. Oldenburg, and Q. Zhou, "CO_2 migration and pressure evolution in deep saline aquifers," *International Journal of Greenhouse Gas Control*, pp. 203–220, 2015.

[5] K. Michael, A. Golab, V. Shulakova et al., "Geological storage of CO_2 in saline aquifers—a review of the experience from existing storage operations," *International Journal of Greenhouse Gas Control*, vol. 4, no. 4, pp. 659–667, 2010.

[6] S. D. Hovorka, S. M. Benson, C. Doughty et al., "Measuring permanence of CO_2 storage in saline formations: the Frio experiment," *Environmental Geosciences*, vol. 13, no. 2, pp. 105–121, 2006.

[7] K. Sato, S. Mito, T. Horie et al., "Monitoring and simulation studies for assessing macro- and meso-scale migration of CO_2 sequestered in an onshore aquifer: Experiences from the Nagaoka pilot site, Japan," *International Journal of Greenhouse Gas Control*, vol. 5, no. 1, pp. 125–137, 2011.

[8] H. Würdemann, F. Möller, M. Kühn et al., "CO_2 SINK-From site characterisation and risk assessment to monitoring and verification: One year of operational experience with the field laboratory for CO_2 storage at Ketzin, Germany," *International Journal of Greenhouse Gas Control*, vol. 4, no. 6, pp. 938–951, 2010.

[9] J. Litynski, S. Plasynski, L. Spangler et al., "U.S. Department of Energy's Regional Carbon Sequestration Partnership Program: Overview," *Energy Procedia*, vol. 1, no. 1, pp. 3959–3967, 2009.

[10] J. Litynski, T. Rodosta, D. Vikara, and R. Srivastava, "U.S. DOE's R&D Program to develop infrastructure for carbon storage: Overview of the regional carbon sequestration partnerships and other R&D field projects," *Energy Procedia*, vol. 37, pp. 6527–6543, 2013.

[11] T. A. Torp and J. Gale, "Demonstrating storage of CO2 in geological reservoirs: The Sleipner and SACS projects," *Energy*, vol. 29, no. 9-10, pp. 1361–1369, 2004.

[12] C. Preston, M. Monea, W. Jazrawi et al., "IEA GHG Weyburn CO_2 monitoring and storage project," *Fuel Processing Technology*, vol. 86, no. 14-15, pp. 1547–1568, 2005.

[13] A. Mathieson, J. Midgely, I. Wright, N. Saoula, and P. Ringrose, "In Salah CO_2 storage JIP: CO_2 sequestration monitoring and verification technologies applied at Krechba, Algeria," *Energy Procedia*, vol. 4, pp. 3596–3603, 2011.

[14] R. J. Finley, S. M. Frailey, H. E. Leetaru, O. Senel, M. L. Couëslan, and S. Marsteller, "Early operational experience at a one-million tonne CCS demonstration project, Decatur, Illinois, USA," *Energy Procedia*, vol. 37, pp. 6149–6155, 2013.

[15] J. M. Nordbotten, M. A. Celia, S. Bachu, and H. K. Dahle, "Semi-analytical solution for CO_2 leakage through an abandoned well," *Environmental Science & Technology*, vol. 39, no. 2, pp. 602–611, 2005.

[16] B. Hof, C. W. H. Van Doorne, J. Westerweel et al., "Experimental observation of nonlinear traveling waves in turbulent pipe flow," *Science*, vol. 305, no. 5690, pp. 1594–1598, 2004.

[17] C. E. Brennen, *Fundamentals of Multiphase Flows*, Cambridge University Press, 2005.

[18] S. E. Ingebritsen, W. E. Sanford, and C. E. Neuzil, "Groundwater in Geologic Processes," Cambridge University Press, New Yourk, NY, USA, Second edition edition, 2006.

[19] E. Lindeberg, "Modelling pressure and temperature profile in a CO_2 injection well," *Energy Procedia*, vol. 4, pp. 3935–3941, 2011.

[20] C. M. Oldenburg, C. Doughty, C. A. Peters, and P. F. Dobson, "Simulations of long-column flow experiments related to geologic carbon sequestration: Effects of outer wall boundary condition on upward flow and formation of liquid CO_2," *Greenhouse Gases: Science and Technology*, vol. 2, no. 4, pp. 279–303, 2012.

[21] M. Lu and L. D. Connell, "Non-isothermal flow of carbon dioxide in injection wells during geological storage," *International Journal of Greenhouse Gas Control*, vol. 2, no. 2, pp. 248–258, 2008.

[22] M. Lu and L. D. Connell, "Transient, thermal wellbore flow of multispecies carbon dioxide mixtures with phase transition during geological storage," *International Journal of Multiphase Flow*, vol. 63, pp. 82–92, 2014.

[23] X. Li, R. Xu, L. Wei, and P. Jiang, "Modeling of wellbore dynamics of a CO2 injector during transient well shut-in and start-up operations," *International Journal of Greenhouse Gas Control*, vol. 42, pp. 602–614, 2015.

[24] L. Pan, C. M. Oldenburg, K. Pruess, and Y.-S. Wu, "Transient CO_2 leakage and injection in wellbore-reservoir systems for geologic carbon sequestration," *Greenhouse Gases: Science and Technology*, vol. 1, no. 4, pp. 335–350, 2011.

[25] D. Liu, Y. Li, L. Xu, and Y. Yu, "Numerical investigation of the influence of interaction between wellbore flow and lateral reservoir flow on CO_2 geological sequestration," *Environmental Earth Sciences*, vol. 74, no. 1, pp. 715–726, 2015.

[26] M. Lu and L. D. Connell, "The transient behaviour of CO_2 flow with phase transition in injection wells during geological storage - Application to a case study," *Journal of Petroleum Science and Engineering*, vol. 124, pp. 7–18, 2014.

[27] W. S. Han, G. A. Stillman, M. Lu, C. Lu, B. J. McPherson, and E. Park, "Evaluation of potential nonisothermal processes and heat transport during CO_2 sequestration," *Journal of Geophysical Research: Solid Earth*, vol. 115, no. 7, Article ID B07209, 2010.

[28] C. M. Oldenburg, "Joule-Thomson cooling due to CO_2 injection into natural gas reservoirs," *Energy Conversion and Management*, vol. 48, no. 6, pp. 1808–1815, 2007.

[29] V. Vilarrasa and J. Rutqvist, "Thermal effects on geologic carbon storage," *Earth-Science Reviews*, vol. 165, pp. 245–256, 2017.

[30] J. Henninges, A. Liebscher, A. Bannach et al., "P-T-ρ and two-phase fluid conditions with inverted density profile in observation wells at the CO_2 storage site at Ketzin (Germany)," *Energy Procedia*, vol. 4, pp. 6085–6090, 2011.

[31] V. Vilarrasa, O. Silva, J. Carrera, and S. Olivella, "Liquid CO_2 injection for geological storage in deep saline aquifers," *International Journal of Greenhouse Gas Control*, vol. 14, pp. 84–96, 2013.

[32] N. Spycher and K. Pruess, "CO_2-H_2O mixtures in the geological sequestration of CO_2. II. Partitioning in chloride brines at 12–100°C and up to 600 bar," *Geochimica et Cosmochimica Acta*, vol. 69, pp. 3309–3320, 2005.

[33] K. Pruess and J. García, "Multiphase flow dynamics during CO_2 disposal into saline aquifers," *Environmental Geology*, vol. 42, no. 2-3, pp. 282–295, 2002.

[34] L. André, Y. Peysson, and M. Azaroual, "Well injectivity during CO_2 storage operations in deep saline aquifers - Part 2: Numerical simulations of drying, salt deposit mechanisms and role of capillary forces," *International Journal of Greenhouse Gas Control*, vol. 22, pp. 301–312, 2014.

[35] G. Bacci, A. Korre, and S. Durucan, "An experimental and numerical investigation into the impact of dissolution/precipitation mechanisms on CO_2 injectivity in the wellbore and far field regions," *International Journal of Greenhouse Gas Control*, vol. 5, no. 3, pp. 579–588, 2011.

[36] J. Oh, K.-Y. Kim, W. S. Han, T. Kim, J.-C. Kim, and E. Park, "Experimental and numerical study on supercritical CO_2/brine transport in a fractured rock: Implications of mass transfer, capillary pressure and storage capacity," *Advances in Water Resources*, vol. 62, pp. 442–453, 2013.

[37] Y. Peysson, L. André, and M. Azaroual, "Well injectivity during CO_2 storage operations in deep saline aquifers-Part 1: Experimental investigation of drying effects, salt precipitation and capillary forces," *International Journal of Greenhouse Gas Control*, vol. 22, pp. 291–300, 2014.

[38] H. Alkan, Y. Cinar, and E. B. Ülker, "Impact of Capillary Pressure, Salinity and In situ Conditions on CO_2 Injection into Saline Aquifers," *Transport in Porous Media*, vol. 84, no. 3, pp. 799–819, 2010.

[39] K.-Y. Kim, W. S. Han, J. Oh, E. Park, and P.-K. Lee, "Flow Dynamics of CO_2/brine at the Interface Between the Storage Formation and Sealing Units in a Multi-layered Model," *Transport in Porous Media*, vol. 105, no. 3, pp. 611–633, 2014.

[40] E. Guyant, W. S. Han, K.-Y. Kim, M.-H. Park, and B.-Y. Kim, "Salt precipitation and CO_2/brine flow distribution under different injection well completions," *International Journal of Greenhouse Gas Control*, vol. 37, pp. 299–310, 2015.

[41] K.-Y. Kim, W. S. Han, J. Oh, T. Kim, and J.-C. Kim, "Characteristics of salt-precipitation and the associated pressure build-up during CO_2 storage in saline aquifers," *Transport in Porous Media*, vol. 92, no. 2, pp. 397–418, 2012.

[42] K. Pruess and N. Müller, "Formation dry-out from CO_2 injection into saline aquifers: 1. effects of solids precipitation and their mitigation," *Water Resources Research*, vol. 45, no. 3, Article ID W03402, 2009.

[43] M. Bahonar, J. Azaiez, and Z. Chen, "Transient nonisothermal fully coupled wellbore/reservoir model for gas-well testing, part 1: Modelling," *Journal of Canadian Petroleum Technology*, vol. 50, no. 9-10, pp. 37–50, 2011.

[44] D. Liu, Y. Li, S. Song, and R. Agarwal, "Simulation and analysis of lithology heterogeneity on CO_2 geological sequestration in deep saline aquifer: a case study of the Ordos Basin," *Environmental Earth Sciences*, vol. 75, pp. 1–13, 2016.

[45] K. Rasmusson, C.-F. Tsang, Y. Tsang et al., "Distribution of injected CO_2 in a stratified saline reservoir accounting for coupled wellbore-reservoir flow," *Greenhouse Gases: Science and Technology*, vol. 5, no. 4, pp. 419–436, 2015.

[46] L. André, M. Azaroual, and A. Menjoz, "Numerical simulations of the thermal impact of supercritical CO_2 injection on chemical reactivity in a carbonate saline reservoir," *Transport in Porous Media*, vol. 82, pp. 247–274, 2010.

[47] T. Giorgis, M. Carpita, and A. Battistelli, "2D modeling of salt precipitation during the injection of dry CO_2 in a depleted gas reservoir," *Energy Conversion and Management*, vol. 48, no. 6, pp. 1816–1826, 2007.

[48] T. J. Tambach, D. Loeve, C. Hofstee, W.-J. Plug, and J. G. Maas, "Effect of CO_2 Injection on Brine Flow and Salt Precipitation After Gas Field Production," *Transport in Porous Media*, vol. 108, no. 1, pp. 171–183, 2015.

[49] L. Pan, B. Freifeld, C. Doughty, and S. Zakem, "Fully coupled wellbore-reservoir modeling of geothermal heat extraction using CO_2 as the working fluid," *Geothermics*, vol. 53, pp. 100–113, 2015.

[50] A. T. Corey, "The Interrelation between gas and oil relative permeabilities," *Producers Monthly*, vol. 19, p. 38, 1954.

[51] M. T. van Genuchten, "A closed-form equation for predicting the hydraulic conductivity of unsaturated soils," *Soil Science Society of America Journal*, vol. 44, no. 5, pp. 892–898, 1980.

[52] S. Goodarzi, A. Settari, M. D. Zoback, and D. W. Keith, "Optimization of a CO_2 storage project based on thermal, geomechanical and induced fracturing effects," *Journal of Petroleum Science and Engineering*, vol. 134, pp. 49–59, 2015.

[53] K. Pruess, C. Oldenburg, and G. Moridis, *TOUGH2 User's Guide, Version 2*, Lawrence Berkeley National Laboratory, Berkeley, Calif, USA, 1999.

[54] L. Pan, N. Spycher, C. Doughty, and K. Pruess, "ECO2N V. 2.0: A New TOUGH2 Fluid Property Module for Mixtures of Water, NaCl, and CO_2," Tech. Rep. LBNL–6930E, 2014.

[55] L. Pan, C. Oldenburg, Y. Wu, and K. Pruess, "T2Well/ECO2N version 1.0: multiphase and non-isothermal model for coupled wellbore-reservoir flow of carbon dioxide and variable salinity water," Tech. Rep. LBNL-4291E, Lawrence Berkeley National Laboratory, Berkeley, Claif, USA, 2011.

[56] K. Pruess, *ECO2N: A TOUGH2 Fluid Property Module for Mixtures of Water, NaCl, and CO_2*, Lawrence Berkeley National Laboratory, Berkeley, Calif, USA, 2005.

[57] H. Shi, J. A. Holmes, L. J. Durlofsky et al., "Drift-flux modeling of two-phase flow in wellbores," *SPE Journal*, vol. 10, no. 1, pp. 24–33, 2005.

[58] P. Jiang, X. Li, R. Xu et al., "Thermal modeling of CO_2 in the injection well and reservoir at the Ordos CCS demonstration project, China," *International Journal of Greenhouse Gas Control*, vol. 23, pp. 135–146, 2014.

[59] A. Verma and K. Pruess, "Thermohydrological conditions and silica redistribution near high-level nuclear wastes emplaced in saturated geological formations," *Journal of Geophysical Research: Atmospheres*, vol. 93, no. 2, pp. 1159–1173, 1988.

[60] D. Zhou, F. J. Fayers, and F. M. Orr, "Scaling of multiphase flow in simple heterogeneous porous media," *Society of Petroleum Engineers*, vol. 12, no. 3, 1997.

[61] S. Taku Ide, K. Jessen, and F. M. Orr Jr., "Storage of CO_2 in saline aquifers: Effects of gravity, viscous, and capillary forces on amount and timing of trapping," *International Journal of Greenhouse Gas Control*, vol. 1, no. 4, pp. 481–491, 2007.

[62] A. Cooksy, *Physical Chemistry Thermodynamics, Statistical Mechanics*, Kinetics, Pearson Education, New Jersey, NJ, USA, 2013.

[63] R. Span and W. Wagner, "A new equation of state for carbon dioxide covering the fluid region from the triple-point temperature to 1100 K at pressures up to 800 MPa," *Journal of Physical and Chemical Reference Data*, vol. 25, no. 6, pp. 1509–1596, 1996.

[64] V. Vilarrasa, J. Carrera, D. Bolster, and M. Dentz, "Semianalytical Solution for CO_2 Plume Shape and Pressure Evolution During CO_2 Injection in Deep Saline Formations," *Transport in Porous Media*, vol. 97, no. 1, pp. 43–65, 2013.

[65] K. Pruess, "Numerical studies of fluid leakage from a geologic disposal reservoir for CO_2 show self-limiting feedback between fluid flow and heat transfer," *Geophysical Research Letters*, vol. 32, no. 14, pp. 1–4, 2005.

[66] W. S. Han, K.-Y. Kim, E. Park, B. J. McPherson, S.-Y. Lee, and M.-H. Park, "Modeling of spatiotemporal thermal response to CO_2 injection in saline formations: interpretation for monitoring," *Transport in Porous Media*, vol. 93, no. 3, pp. 381–399, 2012.

[67] J. Hwang, S. Baek, H. Lee, W. Jung, and W. Sung, "Evaluation of CO_2 storage capacity and injectivity using a relief well in a saline aquifer in Pohang basin, offshore South Korea," *Geosciences Journal*, vol. 20, no. 2, pp. 239–245, 2016.